A Study of Layered Li-Excess Cathode Materials for High-Energy-Density Li-Ion Battery Systems

September 2021

CAO XIN

A Study of Layered Li-Excess Cathode Materials for High-Energy-Density Li-Ion Battery Systems

Graduate School of Systems and Information Engineering

University of Tsukuba

September 2021

CAO XIN

ABSTRACT

Rechargeable lithium-ion batteries can be regarded as efficient devices to storage energy owing to their relatively high energy density and ultralong cycling life. With the evolution of application scenarios form mini mobile phone to large electric vehicles, the increasing requirement of high energy density is further put forward in existing lithium-ion batteries. However, one of the limiting factors of improving the energy density focus on the cathode material. They generally possess the low specific capacity, which is hard to match the that of anodes with high output specific capacity. Consequently, the weight ratio of cathode needs to be further increased to make up the large gap of specific capacity between anode and cathode materials, which greatly decreases the output specific capacity of full battery systems. Therefore, a lot of efforts have been made in developing next-generation cathode materials with excellent electrochemical performance. Herein, Li-rich/excess cathode materials attract much attention because it exhibits higher output capacity triggered by both anionic and cationic redox reactions.

For layered Li-rich/excess oxides, the utilization of anionic oxygen-related redox reactions always suffers from two challenges. The first one is lattice oxygen release. It was caused by the excessive oxidation reactions of lattice oxygen during initial oxygen activation process. Generally, the lattice oxygen is firstly oxidized to peroxide, and then to superoxide, and finally to gaseous oxygen. Furthermore, the formation of oxygen molecule would induce serious capacity loss because it cannot be effectively reduced upon discharge process. Moreover, the lattice oxygen loss accelerates the irreversible transition metal (TM) migration, which is second challenge for layered Li-rich/excess oxides. As a result, the irreversible TM migration induces the harmful phase transition from layered structure to spinel-like phase, which causes serious voltage decay during cycling. To resolve these problems, O2-type Li-excess $Li_{0.66}[Li_{0.12}Ni_{0.15}Mn_{0.73}]O_2$ was developed by the chemical Li^+/Na^+ ion exchange method from P2-type $Na_{0.66}[Li_{0.12}Ni_{0.15}Mn_{0.73}]O_2$. Within the O2-type Li-excess cathode, the layered/spinel

phase transition and irreversible oxygen loss can be effectively restrained, displaying the excellent structural and electrochemical stability during long cycling. As a comparison, a similar O2-type oxide was also prepared by the electrochemical ion exchange from same Na-based precursor. It displayed the inferior electrochemical performance. From the aspect of methodology, chemical ion exchange is an effective route to obtain the O2-type Li-excess cathodes. Besides, the cationic/anionic redox reactions in optimized O2-type layered oxide were clearly assigned and quantified.

On the other hand, a modified O3-type Li-excess layered cathode material, $Li_{0.6}[Li_{0.2}Mn_{0.8}]O_2$, was developed by chemical Li^+/Na^+ ion exchange strategy from P3-type Na-precursor. Compared with typical O3-type Li-rich layered oxides, the TM layer in LMO still displays Li-excess state, while the alkali metal (AM) layer exhibits Li-deficient state. By means of low Li content in AM layer, the oxidized lattice oxygen produced upon charging can be well reduced to lattice oxygen during subsequent discharging. Furthermore, by achieving the Li substitution within TM layer, the high specific capacity of 329 mAh g^{-1} can be realized, which is beneficial for achieving high-energy-density battery systems. Moreover, by employing spectroscopic characterization systems, the charge compensation mechanism of complex Mn-based and O-related redox reactions can be clearly clarified during charging and discharging processes. Besides, the reversible structure evolution and Li migration can be obtained, which provides a solid foundation for long cycle life of battery systems.

Our findings provide a guide for the design of excellent Li-rich/excess materials from the aspect of structural optimization, in which the challenges of oxygen release and irreversible TM migration can be resolved. Moreover, the deep insights for anionic and cationic redox behaviors are pointed out from the mechanism aspect.

TABLE OF CONTENTS

LIST OF FIGURES

LIST OF TABLES

Chapter 1. General introduction

1.1 The development of renewable energy and the applications of Li-ion battery systems

Although the application of fossil energy has greatly promoted the development of our society, these traditional resources are increasingly depleting.[1] At the same time, the excessive consumption of fossil energy has induced serious environmental pollution and climate problems. Many countries around the world have put forward the future energy strategy of increasing the proportion of renewable energy to achieve the goal of carbon neutrality and reduce the dependence on traditional energy sources.[2] By means of the energy harvesting devices such as solar energy and wind turbine, the inexhaustible resources can be well exploited to supply energy for devices such as laptop, electric vehicles, and home applications, where the process is clean and environmentally friendly.[3] The relationship between the renewable energy and the applications is also depicted in **Figure 1.1**.

Figure 1. 1 Energy exploited from solar panels and wind turbines for home applications. Picture was collected from https://www.freepik.com/free-vector/engineer-choosing-power-station-with-solar-panels-wind-turbines_12085760.html. Retrieved March 21, 2021.

As described above, solar and wind energy as typical renewable energy sources are widely employed in our society. However, the utilization of these renewable energy is always limited by local weather and regional climate. That means that these conversion systems only can produce the energy without the ability of energy storage. Thus, it is

impending to build a stable and effective device to store renewable energy and provide energy for external applications when it required.[4-5] Herein, the Li-ion batteries can be regarded as a key medium or bridge between renewable energy and electronic applications.[6-7] The Li-ion battery systems have been diffusely employed in many energy storage devices and systems such as mobile phone, electric vehicle, and residential storage application, which consists an essential part for daily activities. Besides, Li-ion battery systems are also widely utilized in many fields, including telecommunications, electrical vehicles, railways, space applications etc.[4] With the evolution of application scenarios form mobile phone to electric vehicles even to residential storage systems, the requirement of high energy density is further put forward in existing Li-ion battery systems, which is also shown in **Figure 1.2**. Especially for electric vehicles, the battery technology should be improved to meet the high requirements of volumetric and gravimetric energy density.[8] Although the Li-ion batteries have many advantages such as high safety, stability, and long life compared with other battery technologies, the energy density needs to be further improved to match the growing demands in complicated situations.[9]

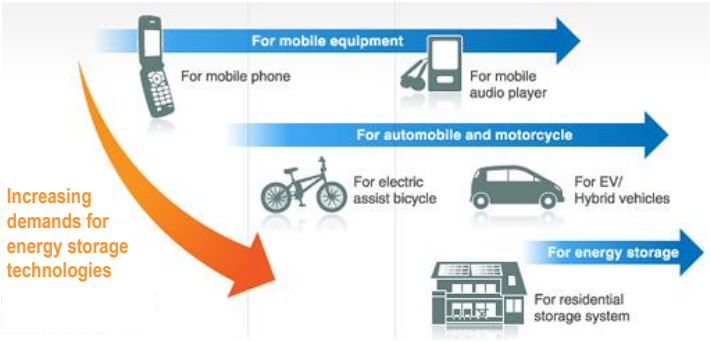

Figure 1. 2 The development of Li-ion batteries within many commercialization applications. Picture was from http://tr-nec-com-org.onenec.net/en_TR/global/environment/energy/nec_aes/index.html. Retrieved April 6, 2021.

1.2 The working mechanism of Li-ion battery systems

To further promote the energy density of existing Li-ion batteries, it is necessary to know the working mechanism at first. The schematic of Li-intercalation/extraction mechanism is shown in **Figure 1.3a**. The typical battery generally consists of four parts

including layered $LiCoO_2$ as cathode material, Li salts in carbonates as electrolyte, graphite as anode material, and separator. Upon charging process, Li^+ ions extracted from $LiCoO_2$ and migrated to graphite by electrolyte. Subsequently, upon the discharge process, equivalent Li ions migrated from anode back to cathode side, which provides electrons for external circuit. The charge and discharge processes are reversible accompanied by Li^+ ions migration between cathode and anode. Therefore, the reversible electrochemical reactions also were achieved based on reversible Co and C redox reactions.

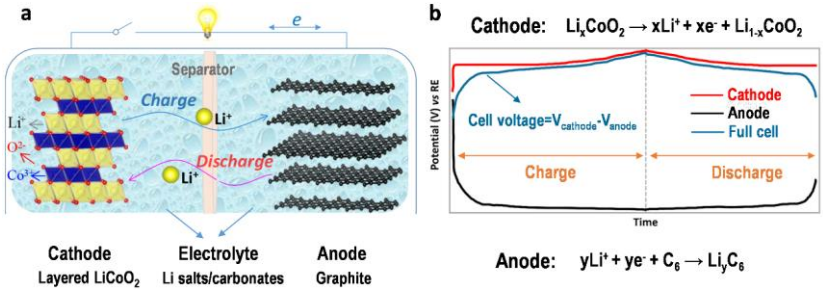

Figure 1. 3 a) The Li-intercalation/extraction mechanism of Li-ion batteries. b) Charge and discharge profiles of $LiCoO_2$ and graphite in Li half-cell as well as the $LiCoO_2$/Graphite full cell.[10] Reproduced with permission from ref. 10. Copyright 2019, MDPI.

According to charge/discharge curves of $LiCoO_2$ and graphite in Li half-cell as well as the $LiCoO_2$/Graphite full cell shown in **Figure 1.3b**, it is not hard to find that the charge/discharge profiles of full cell can be generated from the difference between anode and cathode profiles.[10] Therefore, the voltage of full cell can be calculated as the difference between cathode and anode potentials. Owing to the same number of transfer electrons between two electrodes, the specific capacity of full cell depends on that of both cathode and anode materials. Herein, the output energy density (Wh kg^{-1}) of the full cell is obtained by the product of output voltage (V) and specific capacity (mAh g^{-1}). Therefore, the energy density of full battery system mainly determined by the cell voltage and specific capacity. Therefore, there are two strategies to improve the energy density. The first strategy is enlarging the voltage difference between two electrodes. The other strategy is improving the specific capacity of both cathodes and anodes.

1.3 An overview of available electrodes of Li-ion battery systems

1.3.1 Typical anode materials for Li-ion batteries

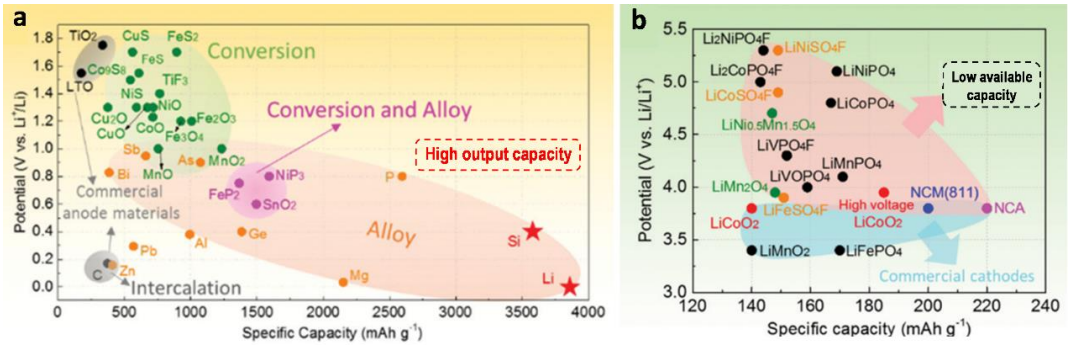

Figure 1. 4 The summary of a) anode and b) cathode materials with estimated work potentials and specific capacity.[12] Reproduced with permission from ref. 12. Copyright 2020, Royal Society of Chemistry.

To improve the energy density, the output voltage and specific capacity should be increased at the same time. For anode materials, it should meet the standards of low working potential and high output capacity.[11] Herein, the typical anodes with specific capacity and potential (vs. Li^+/Li) are shown within **Figure 1.4a**.[12] According to the different mechanisms, these selected electrodes are generally classified as intercalation/extraction-, conversion- and alloy-type anode materials. Among them, both graphite and lithium titanate ($Li_4Ti_5O_{12}$, labelled as LTO) are well-known commercial anode materials, in which they follow intercalation/extraction mechanism to store energy. The layered graphite stored 1 mol Li^+ ions per 6 mol C by intercalating Li atoms in graphene planes, which provides a theoretical capacity of 372 mAh g^{-1}.[13] Furthermore, spinel LTO possesses the ability of rate performance and long cycling life because of the zero-strain effect during (de)intercalation processes.[14] Furthermore, conversion- and alloy-type anode materials typically exhibit high theoretical capacity, which exceeds that of commercial anodes. For instance, conversion-type Fe_2O_3 harvests the theoretical capacities of 1007 mAh g^{-1} based on conversion mechanism.[15] Compared with conversion-type anodes, alloy-type materials are suitable anode

candidates since it has higher specific capacity and relatively lower work voltage. For example, Li metal and silicon anode display the low working potential and high-theoretical-capacity of 3860 and 4200 mAh/g, respectively. [16-17] These alloy-type anode materials mainly come from IV group such as Si and Ge, or V group including P and Sb, or some light metals such as Mg and Al, which provides optimized options and attracting perspectives for high-energy-density Li-ion battery systems.[18]

1.3.2 Typical cathode materials for Li-ion batteries

The oxide cathodes are generally classified into layered, spinel and polyanion-type materials according to their structural characteristics. The most typical layered cathode is $LiCoO_2$, where the Co^{3+} ions are arranged within the TM layer and Li^+ ions occupy octahedral sites the Li layer.[19] As shown in **Figure 1.5**, the typical layered structure consists of two-dimensional LiO_6 and CoO_6 slabs, which displays the alternately layer-by-layer arrangement.[20] The layered structure is defined as O3-type structure. The layered $LiCoO_2$ offers the specific gravimetric capacity of ≈180 mAh g^{-1}, and operating voltage of ≈3.8 V.[21] Besides, the commercialized Ni-rich layered oxides such as $LiNi_{0.8}Co_{0.1}Mn_{0.1}O_2$ and $LiNi_{0.8}Co_{0.15}Al_{0.05}O_2$ harvest the capacity of 200 and 220 mAh g^{-1}, respectively.[22] In general, the layered oxides always exhibit higher discharge capacity than that of other structures. For spinel-type cathode materials, the classic $LiMn_2O_4$ cathode is arranged as that Li is located at 8a tetrahedral site and $Mn^{3+/4+}$ ions occupy the 16d octahedral sites. It has the operating voltage of around 4.0 V with an available capacity of lower than 130 mAh g^{-1}.[23] By means of Ni substitution, the spinel $LiNi_{0.5}Mn_{1.5}O_4$ displays the high operating potential of 4.7 V and specific capacity of 147 mAh g^{-1}.[24] Unlike previous two oxides with simple structure, polyanionic compounds consist of phosphates and sulfates. The output capacity of polyanionic compounds generally is lower than ≈170 mAh g^{-1}. For instance, the commercialized $LiFePO_4$ electrode has many advantages including the low cost, stable long cycle, and high safety. However, it possesses the disadvantages of low electronic conductivity and low specific capacity.[25] Thus, the available discharge capacity of these cathode

materials shown in **Figure 1.4b** generally is lower than ≈220 mAh/g, which is not beneficial for achieving high-energy-density Li-ion batteries.

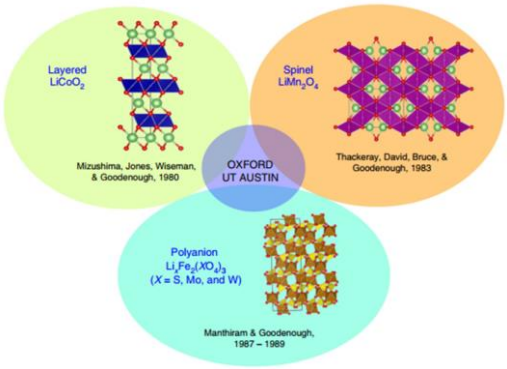

Figure 1. 5 The chemical formulas and structures of classic layered, spinel and polyanion oxide cathode materials.[26] Reproduced with permission from ref. 26. Copyright 2020, Nature Publishing Group.

Owning to the large gap of specific capacity between anode and cathode materials, the weight ratio of cathode needs to be further increased to make up for the disadvantages of low capacity, which greatly decreases the output specific capacity in battery systems. For example, the available capacity of graphite is ≈360 mAh g^{-1}, whereas the available capacity of $LiCoO_2$ is about 140 mAh g^{-1}. Therefore, the weight of cathode in full cell is 2.57 times that of anode, which is used for satisfying the charge balance. Therefore, the limiting factor to achieve high-energy-density batteries mainly lies in the cathode side.

1.4 Li-rich/excess oxides for Li-ion batteries

1.4.1 The electrochemical performances of conventional layered oxides and Li-rich/excess oxides

The comparisons of typical specific discharge capacity and energy density between layered Li-rich/excess cathodes and other conventional oxides is shown in **Figure 1.6a** and **1.6b**, respectively. Compared with the discharge curves of conventional cathodes, the layered Li-rich/excess oxides exhibit high output capacity of more than 300 mAh g^{-1} and relatively high average voltage.[27] These typical layered Li-rich/excess oxides

generally display higher discharge capacity than conventional layered oxides such as $LiCoO_2$ and $LiNi_{0.85}Co_{0.1}Al_{0.05}O_2$.[28] The discharge capacities of typical layered Li-rich/excess oxides are suitable for matching that of commercial anode such as graphite. In the full battery systems, the combination of Li-rich/excess oxide as cathode and graphite as anode can provide more than 1100 mWh cm^{-3}, which exceeds that of most current battery systems by using $LiFePO_4$, $LiCoO_2$, $LiNi_{1/3}Mn_{1/3}Co_{1/3}O_2$ and $LiNi_{0.85}Co_{0.1}Al_{0.05}O_2$ as cathode materials.[29] Therefore, Li-rich/excess cathodes are widely considered as promising candidates for high-energy-density Li-ion batteries since it processes high output capacity with relatively high average voltage. Compared with other conventional layered oxides, they always display Li-rich or Li-excess state. The Li-rich state means the ratio of Li/TM is larger than 1, whereas the ratio in conventional layered oxides is 1. Moreover, the Li-excess state means Li substitution exists within TM layer.[30] Both Li-excess and Li-rich cathode materials can harvest the large capacity triggered by anionic and cationic redox reactions simultaneously.[31]

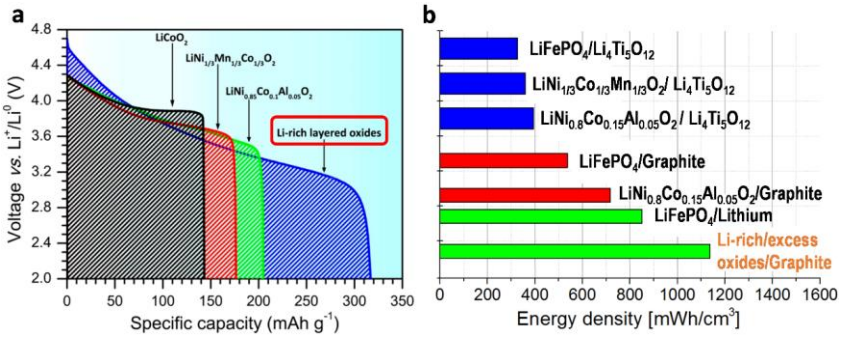

Figure 1. 6 a) The discharge profiles of conventional cathode materials and Li-rich oxides with b) a summary of energy density of full cells constructed by Li-rich/excess oxides and other advanced cathodes with the corresponding anodes.[29, 32] Reproduced with permission from ref. 29. Copyright 2018, American Chemical Society. Reproduced with permission from ref. 32. Copyright 2017, American Chemical Society.

1.4.2 The structure difference between conventional and Li-rich/excess layered oxides

To understand the difference of electrochemical behaviors between conventional and

Li-rich/excess layered oxides, the structure difference should be clarified at first. Herein, the layered structures of conventional $LiMO_2$ (M: metals) and Li-rich Li_2MnO_3 are shown in **Figure 1.7a**. The schematic diagrams of two layered oxides are consist of Li ions (green), metal atoms (purple) and oxygen atoms (red). Viewed from the c-axis direction, the compositions of both conventional $LiMO_2$ and Li-rich Li_2MnO_3 are repeating sequences of a TM layer, an oxygen layer, a Li layer, an oxygen layer, and a TM layer.[33] The conventional $LiMO_2$ possesses the space group of trigonal $R\bar{3}m$, whereas the space group of Li-rich Li_2MnO_3 is monoclinic *C/2m*. Despite the Li-rich Li_2MnO_3 displayed the same stacking arrangement as $LiMO_2$, the excess Li occupies the Mn site within the TM layer, which is an obvious difference between two layered structures. In the ab plane, the arrangement of Li and metal atoms in TM layer can be arranged in a hexagonal pattern, which is shown in **Figure 1.7b**.[34] In the TM layer of conventional $LiMO_2$, all atomic sites (gray) are occupied by TM without other atoms. For Li-rich Li_2MnO_3, the excess Li occupies the S1 sites and has ordered arrangement with Mn atoms, which produces the configuration of Li-O-Li along c-axis direction. Therefore, the Li substitution within TM layer generates Li-O-Li configuration in Li-rich oxide, which is a significant structural difference with conventional layered oxides.

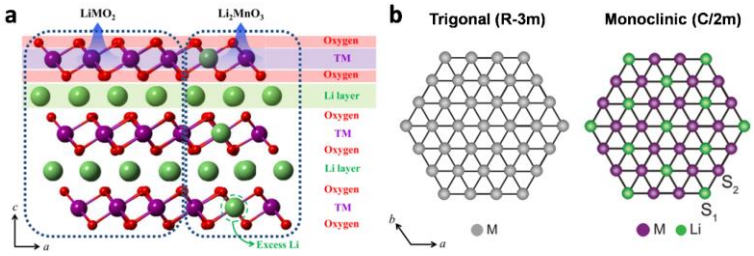

Figure 1. 7 Crystal structural schematic diagrams of conventional layered $LiMO_2$ cathodes and Li-rich Li_2MnO_3 viewed a) along c-axis direction and b) in ab plane.[33-34] Reproduced with permission from ref. 33. Copyright 2011, American Chemical Society. Reproduced with permission from ref. 34. Copyright 2015, Elsevier.

1.4.3 The mechanism of oxygen redox reactions in Li-rich/excess oxides

Compared with the structure of conventional layered oxides, the significant Li-O-Li configuration can be generated within Li-rich Li_2MnO_3, which is important to clarify

the underlying mechanism that oxygen redox reactions can be achieved within Li-rich oxides instead of conventional layered cathodes. To better understand the structure difference at molecular level, the neighboring configurations of oxygen and the corresponding schematic band structures of conventional layered oxides and Li-rich A_2MO_3 are shown in **Figure 1.8**. As depicted in **Figure 1.8a**, the chemical formula of conventional layered cathode material is AMO_2 (A: Li^+ ions), in which the layered structure can be classified in trigonal O3-type with $R\bar{3}m$ space group. For conventional layered oxide, oxygen atom was coordinated by three Li^+ ions and three metal ions (such as Ni^{3+}, Co^{3+} Mn^{3+}, etc.). The hybridization of O 2p and M nd orbitals is easily generated since the M (n+1)s/(n+1)p orbitals have high energy compared with O 2p and M nd orbitals. In the configuration of A_3M_3 without Li-O-Li configuration, the hybridization of O 2p and M (n+1)s/(n+1)p orbitals generates the molecular with a_{1g}/t_{1u} and a_{1g}^*/t_{1u}^* orbital. Furthermore, the hybridization of O 2p and M nd (e_g) orbitals produces the σ bonds of e_g and e_g^*.[35] But the M nd (t_{2g}) orbital is at nonbonding state. Thus, the O 2p feature depends on the bonding orbitals, while the M (n+1)s, M(n+1)p and M nd orbitals are at antibonding states. Because the Fermi level within conventional layered oxide is located at e_g^* or t_{2g}, the region was determined by M nd orbital. Therefore, cationic redox reactions mainly contribute to the capacity. Despite the hybridization would generate delocalized holes, the electrons obtained from O 2p are preferably to create the bond at lower energy. Thus, the charge capacity within conventional oxide generally provided by the cationic oxidation reactions.

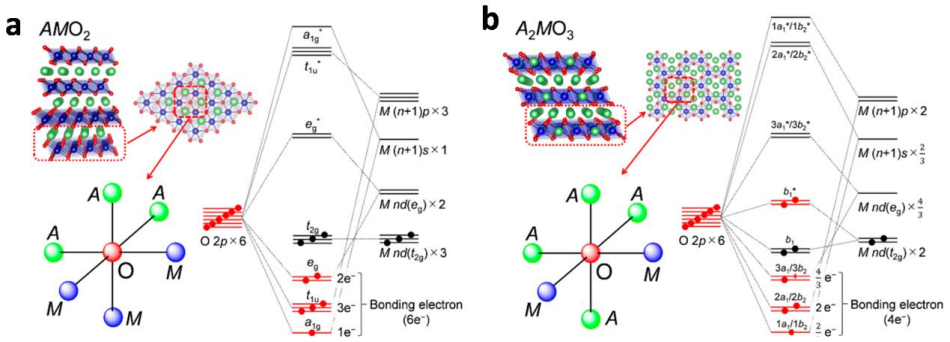

Figure 1. 8 Molecular orbital energy diagrams of a) conventional AMO_2 and b) A-excess A_2MO_3.[35]

Reproduced with permission from ref. 35. Copyright 2017, American Chemical Society.

Li-rich/excess oxides generally break through the traditional capacity limitation by introducing oxygen redox chemistry. For layered Li-rich/excess oxides, oxygen atom has different coordination environment, in which 4 Li^+ ions and 2 metal ions (A_4M_2), forming the significant Li-O-Li configuration along the c-axis direction.[36] For example, within Li-rich Li_2MnO_3, the occupied M nd (t_{2g}) has lower energy level compared with O 2p orbital. Thus, occupied b_1^* orbital consist of O 2p, which is in charge of the oxygen oxidation reactions.[35] Besides, not only the Li-O-Li configuration can trigger oxygen redox reactions, but also the substitution of vacancies or other light elements can harvest the excess capacity from anionic redox reaction. [37-39]

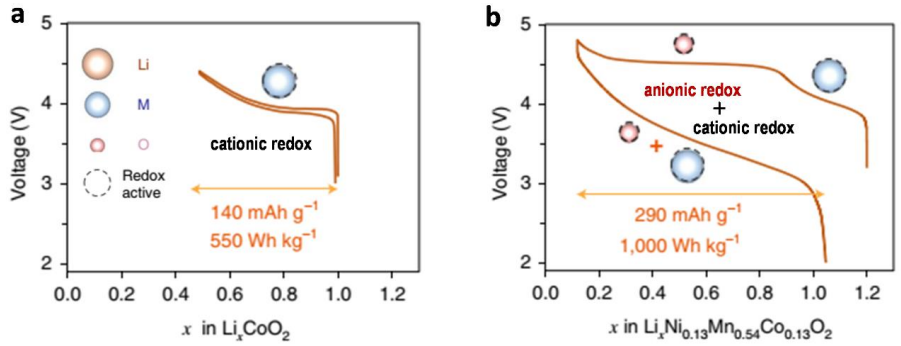

Figure 1. 9 The charge/discharge profiles of a) conventional layered $LiCoO_2$ based on cationic redox reactions and b) Li-rich layered $Li_{1.2}Ni_{0.13}Mn_{0.54}Co_{0.13}O_2$ based on cumulative anionic and cationic redox processes.[40] Reproduced with permission from ref. 40. Copyright 2018, Nature Publishing Group.

Conventional layered cathode materials such as $LiCoO_2$ store and output electrical energy by reversible Li^+ extraction and insertion via cationic redox reactions upon charge and discharge processes. The output capacity of these conventional oxides is limited by the capacity offered by the cationic redox reactions. For example, $LiCoO_2$ electrode harvested the reversible capacity of approximate 140 mAh g^{-1} during Li^+ extraction/insertion processes, delivering the energy density of 550 Wh kg^{-1}. For Li-rich/excess oxides such as $Li_{1.2}Ni_{0.13}Mn_{0.54}Co_{0.13}O_2$, the combination of cationic TM-based and anionic oxygen-related redox reactions within the same material can overcome the specific capacity limit of current electrode materials. For example, by

adding the oxygen redox reactions, the high output capacity of 290 mAh g^{-1} can be obtained, displaying the high energy density of 1000 Wh kg^{-1}.[40] Therefore, the layered Li-rich/excess oxides are generally regarded as the most promising cathode materials for the Li-ion batteries.

By investigating the electrochemical behaviors of two cathodes, $LiCoO_2$ electrode exhibits reversible charge and discharge profiles during first Li^+ (de)intercalation processes, which is consist with pervious works of conventional layered oxides. However, Li-rich $Li_{1.2}Ni_{0.13}Mn_{0.54}Co_{0.13}O_2$ electrode represents a slope region and an obvious plateau at approximate 4.7 V upon charging process, which corresponds to the TM oxidation reactions in lower voltage region and oxygen activation process in higher voltage region.[40] It is not hard to find that the oxygen-related redox reactions provide much capacity during both charge and discharge processes, which greatly improves the capacity and energy density of Li-rich/excess cathode materials. Besides, compared with cationic redox reaction, the anionic redox reactions such as can provide higher specific capacity for battery systems because anionic elements generally have lower molar mass than that of cationic transition metals. For instance, the energy of 26760 mAh (corresponding to 1 mol electron) requires 54.9 g Mn based on cationic redox reaction between Mn^{3+} and Mn^{4+}, whereas about 16 g O can provides same energy based on anionic O^{2-}/O^- redox reaction. Therefore, anionic redox reactions can supply high specific capacity in Li-rich/excess materials.

1.5 The challenges in layered Li-rich/excess materials

1.5.1 Lattice oxygen loss

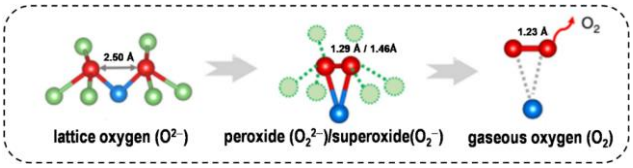

Figure 1. 10 The typical evolution of oxidation reactions from lattice oxygen to peroxide, and then to superoxide, final to O_2 during Li^+ ions deintercalation process.[41] Reproduced with permission from ref. 41. Copyright 2020, Nature Publishing Group.

The utilization of anionic redox behaviors in Li-rich/excess cathodes always suffer from two challenges. The first challenge is lattice oxygen loss. The lattice oxygen loss in Li-rich/excess oxides is generally believed to be generated by the excessive oxidation reactions. As shown in **Figure 1.10**, the oxygen loss process can be described as lattice oxygen is firstly oxidized to peroxide, and then to superoxide, and finally to gaseous oxygen molecules. With the neighboring Li^+ ions removing from oxygen during charging process, the O–O distance shortens sharply. For example, the O–O distance of lattice oxygen is 2.50 Å, in which the value decreased to 1.46 and 1.29 Å when it transformed to peroxide (O^-) and superoxide (O_2^-), respectively.[41] The gaseous oxygen molecule with low O–O distance of 1.23 Å is hard to be reduced during discharge process because neutral oxygen molecule with less occupied antibonding π* orbital is stable. The reaction pathway of oxygen oxidation reactions involves two directions, in which the one is in ab plane and the other is along c-axis direction, as shown in **Figure 1.11**.[42]

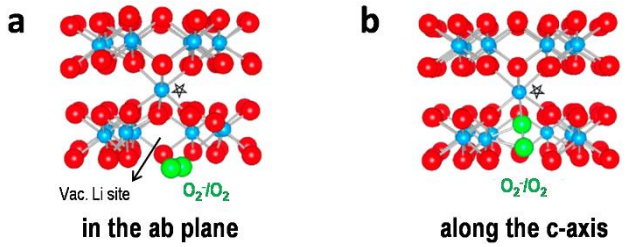

Figure 1. 11 Reaction pathways of oxygen dimerization and phase transformation in Li-rich/excess materials. The pathways with O–O configuration a) in the ab plane and b) along the c-axis.[42] Reproduced with permission from ref. 42. Copyright 2016, American Chemical Society.

The decreasing of O-O distance causes the formation of oxygen release and TM migration upon charging. The formation of oxygen molecule would induce serious capacity loss because it cannot be effectively reduced during discharging. As displayed in **Figure 1.12a**, the Li-rich Li_2MnO_3 electrode displays the serious oxygen loss during first charge process, in which the capacity triggered by oxygen loss reaches about 70 % total charge capacity upon charging.[43] The corresponding capacity is close to the four electron reactions from lattice oxygen (O^{2-}) to oxygen gas (O_2). As depicted in **Figure**

1.12b, the Li_2MnO_3 electrode displays a charming charge capacity of more than 400 mAh g^{-1} triggered by pure oxygen oxidation.[44] However, only a small part of the oxygen-related capacity in the Li_2MnO_3 electrode can be reduced, delivering the irreversible capacity of 224 mAh g^{-1} during discharging process. It combines the Mn and oxygen reduction reactions at same time. It means the reversible capacity contributed by oxygen reduction reactions is great lower than the discharge capacity. For cathode materials, the output specific capacity corresponds to the value of discharge specific capacity, which is significant for the improvement of energy density. Therefore, the first challenge for excellent Li-rich/excess materials is resolving the serious oxygen release during charging processes.

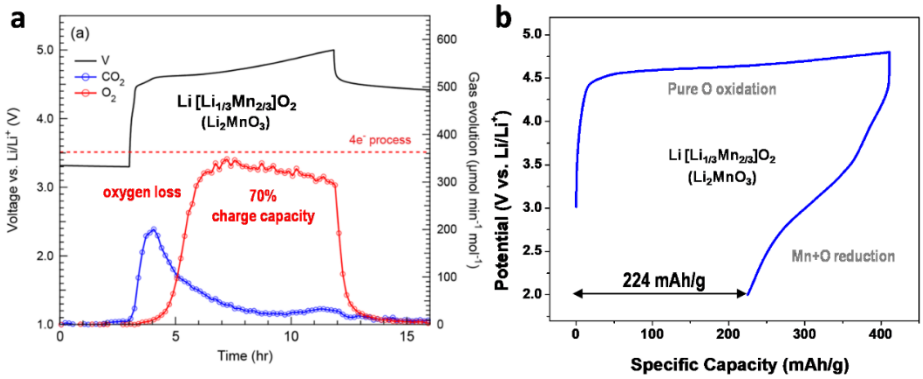

Figure 1. 12 (a) Gas evolution of Li-rich Li_2MnO_3 determined by in-situ differential electrochemical spectrometry upon the first cycle.[43] (b) The typical charge/discharge profiles of Li-rich oxide Li_2MnO_3 upon the initial cycle. Reproduced with permission from ref. 43. Copyright 2020, American Chemical Society.

1.5.2 Irreversible TM migration to Li layer

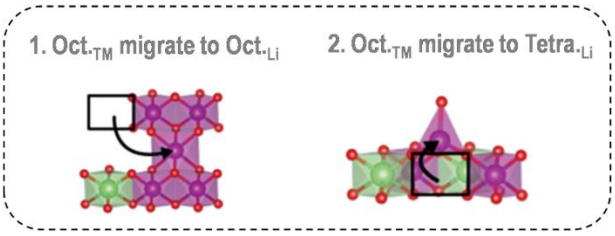

Figure 1. 13 The schematic of the pathways in layered structures of transition metals migrating into octahedral site or tetrahedral site in the Li layer.[47] Reproduced with permission from ref. 47. Copyright 2021, American Chemical Society.

The second challenge for layered Li-rich/excess cathodes is irreversible TM migration to Li layer. The irreversible TM migration can be observed within conventional layered oxides because of similar atomic radius between Li^+ ions and TM ions. For instance, the Li/Ni cationic mixing and further the formation of spinel-like phase caused by irreversible TM migration can be detected in the layered Ni-rich layered oxides upon cycling.[45] For Li-rich/excess materials, the O_2 formation decreased the intensity of TM−O bond, which provides the low energy barrier for TM migration. Therefore, the lattice oxygen loss during charging would accelerate the irreversible TM migration to Li layer. As a result, the formation of spinel phase caused by TM migration can be observed in Li-rich/excess oxides upon the initial several cycles.[46] As displayed in **Figure 1.13**, the reaction pathways of TM migration also have two locations.[47] The first is octahedral site within AM layer and the other is tetrahedral site within AM layer.[48] However, upon discharging, TM ions is hard to reversibly return to the octahedral site within TM layer, which causes the serious structural distortion.

As depicted in **Figure 1.14a**, the obvious structural rearrangement occurred in the Li-rich $Li_{1.2}Mn_{0.55}Ni_{0.15}Co_{0.1}O_2$ electrode at charge state, which is proved by the Transmission Electron Microscope (TEM) results.[49] It is not hard to find the spinel phase exists in the bulk material. The structural rearrangement of layered/spinel transition was caused by the irreversible TM migration. The phase transition would further induce the serious electrochemical decay during cycling. For example, the Li-rich $Li_{1.2}Ni_{0.2}Mn_{0.6}O_2$ electrode suffered from the irreversible TM migration and induced phase transition, resulting in obvious energy loss after 20 cycles because of the capacity loss and voltage fade.[50] The voltage fade occupies more than 65 % in all energy fade, which is the main reason for the energy decay for Li-rich/excess oxides during long-term cycling. Therefore, irreversible oxygen redox reactions facilitate the irreversible TM migration, resulting in the formation of spinel phase after several cycles.

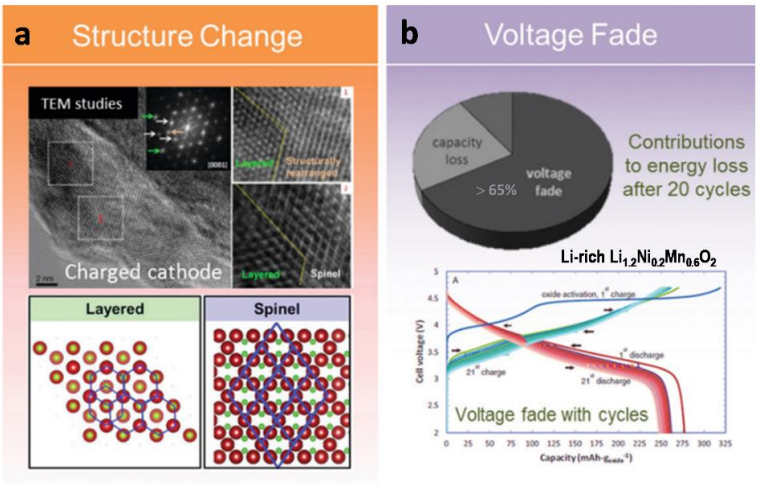

Figure 1. 14 a) Irreversible structure change in Li-rich $Li_{1.2}Mn_{0.55}Ni_{0.15}Co_{0.1}O_2$ during lithiation and de-lithiation. b) Voltage fading in Li-rich $Li_{1.2}Ni_{0.2}Mn_{0.6}O_2$ with several cycles and the distributions of energy loss.[12] Reproduced with permission from ref. 12. Copyright 2020, Royal Society of Chemistry.

1.6 Motivation and targets of this dissertation

1.6.1 Motivation of this dissertation

In recent decades, Li-ion battery systems are well developed as efficient storage devices to storage and output energy for many applications. Moreover, with the increasing requirement of high energy density, the existing Li-ion battery systems should be further improved. The energy density of batteries is mainly determined by cell voltage and specific capacity. Until now, the available specific capacities of commercial cathodes were generally lower than 220 mAh g^{-1}. The low available specific capacity is hard to suitably match the anodes in full cells.

In comparison with available cathodes such as spinel $LiMn_2O_4$, olivine $LiFePO_4$ and layered $LiCoO_2$, Li-rich/excess oxides are generally regarded as promising cathodes for high-energy-density Li-ion battery systems due to it processes high output capacity triggered by anionic/cationic redox reactions. For example, the O3-type Li-rich layered oxides, $xLi_2MnO_3 \cdot (1-x)LiTMO_2$ (TM = Mn, Ni, Co and etc.), generally possess the specific capacity more than 250 mAh g^{-1}. Compared with traditional layered oxide materials, the anionic redox behaviors can be triggered in layered Li-

rich/excess oxides when TM ions are partly replaced by Li^+ ions. Therefore, several Li-rich/excess materials break the capacity bottlenecks only derived from traditional TM-centered redox reactions, which is beneficial for achieving the target of high-energy-density Li-ion battery systems.

However, Li-rich/excess oxides always suffer from the problems of continuous capacity deterioration and voltage decay, which hinders the practical application. The oxygen release and structural distortion are main reasons for performance degeneration. More specifically, lattice oxygen loss in Li-rich/excess material is serious upon the first charge, which is caused by the excessive oxidation reactions. The formation of oxygen molecule would induce serious capacity loss because it cannot be utilized during discharging. Furthermore, the oxygen release would accelerate the harmful structure distortion induced by irreversible TM migration. As a result, the layered structure is severely destroyed and transformed to spinel structure, which causes the continuous voltage decay and capacity loss during long-term cycling.

1.6.2 Targets of this dissertation

The first target is restraining irreversible TM migration within Li-rich/excess oxide materials. The layered Li-rich/excess oxides generally have O3-type structure with oxygen arrangement of ABCABC. The O means the Li ions occupies octahedral sites in Li layer, where the number provides to the repeat period of the TM layer in a unit. Although many research works obtained the performance improvement by doping and coating strategies, these modifications are generally based on the O3-type Li-rich/excess oxide materials. There is a lack of structural design and modification strategies for Li-rich/excess oxide materials. Herein, we designed the novel O2-type Li-excess oxide cathode with ABAC oxygen stacking to solve the issue of irreversible TM migration. The irreversible TM migration can be effectively suppressed in conventional layered O2-type oxides. Therefore, we want to expand the advantage to layered Li-excess oxides.

The second target is resolving the lattice oxygen release upon the first oxygen

activation process. The Li-rich/excess cathodes always suffer from the lattice oxygen loss during charging processes. Especially during the first oxygen activation process, the oxygen release is the most serious, resulting in limited reversible capacities during first discharge process. Furthermore, the oxygen loss inevitably accelerates harmful layered/spinel phase transition induced by irreversible TM migration, which causes the electrochemical decay during long-term cycling. Therefore, it is crucial to restrain the serious oxygen loss, especially for the first oxygen activation process. Here, we modified the O3-type structure with Li-excess state within TM layer and Li-deficient state within AM layer, which not only can utilize oxygen-related capacity, but also can resolve the serious oxygen release during first oxygen activation process.

1.6.3 Outline of this dissertation

Chapter 1 is an introduction part for the dissertation. At first, the applications of Li-ion battery and the typical working mechanism are introduced. Furthermore, the structure features and electrochemical behaviors of conventional layered cathodes and Li-rich oxides are comprehensively compared. Moreover, the challenges for layered Li-rich/excess materials are pointed out. At last, the targets and motivations as well as strategies of this dissertation are put forward.

Chapter 2 introduces the experiment parts of Chapter 3 and Chapter 4. The chapter includes the material preparation, the characterizations of structural and electrochemical tests measurement conditions, and highlights of Chapter 3 and Chapter 4 are presented.

In the Chapter 3, we developed a novel O2-type Li-excess layered oxide, $Li_{0.66}[Li_{0.12}Ni_{0.15}Mn_{0.73}]O_2$ (LLNMO), obtained from the P2-type Na-based precursor $Na_{0.66}[Li_{0.12}Ni_{0.15}Mn_{0.73}]O_2$ (NLNMO) by chemical Li^+/Na^+ ion exchange strategy. Benefiting from the special oxygen stacking of ABAC, the layer-to-spinel phase transition is effectively suppressed within this O2-type structure, displaying the excellent structural and electrochemical stability during long cycling. As a comparison, a similar O2-type oxide was also prepared by the electrochemical ion exchange from

same Na-based precursor. It displayed the inferior electrochemical performance. We demonstrate that chemical ion exchange is an effective strategy to obtain stable structure and pure phase from the aspect of methodology.

In the Chapter 4, we modified the O3-type structure from Li-rich state to Li-deficient in AM layer, which can effectively resolve the lattice oxygen loss during first oxygen activation. The unique O3-type Li-excess layered cathode material, $Li_{0.6}[Li_{0.2}Mn_{0.8}]O_2$ (LMO), was developed by chemical ion exchange strategy. Compared with O3-type Li-rich oxides, the AM layer displays Li-deficient state, while TM layer displays Li-excess state. Benefitting from the modified O3-type structure, the lattice oxygen release is effectively restrained during charge processes. Furthermore, the reversible structure evolution and Li migration process can be obtained. As a result, high discharge capacity and excellent electrochemical stability have been successfully achieved.

Chapter 5 displays the general conclusions, limitation, and perspective for Li-excess oxide cathode materials.

Chapter 2. Experimental section

2.1 Experimental section in Chapter 3

2.1.1 Synthesis of P2-type NLNMO

Na-based P2-type NLNMO cathode material was prepared by solid-state reactions form Na_2CO_3, Li_2CO_3, NiO and MnO_2 of stoichiometric amounts with an excess of 2 mol % Li_2CO_3 and Na_2CO_3 that were ball milled altogether for 24 h at the speed of 350 rpm. Moreover, the mixed powder was pelleted under the pressure of 2 MPa. Furthermore, it was calcined at 700 °C for 20 h in air. After quenching, the Na-deficient precursor NLNMO was stored in the glove box to further ion exchange and electrode preparation. All raw materials are purchased from the Wako company.

2.1.2 Synthesis of O2-type LLNMO

Li-based O2-type LLNMO was prepared by facile chemical ion exchange from Na-based NLNMO in molten salt. Firstly, the NLNMO and 10 times Li-excess salts (88 % $LiNO_3$ and 12 % LiCl with mol ratio) milled altogether for 30 min. Then, the mixture put into furnace and the reaction was performed at 280 °C in air for 1 h. After alternative ion exchange with equivalent Li, LLNMO can be obtained after washing with deionized water and dried at 80 °C for 12 h. All raw materials are purchased from the Wako company.

2.1.3 Characterizations

The structure of the Na-based NLNMO and Li-based O2-type LLNMO were investigated by XRD (Ultima III, Rigaku Corporation) radiation from Cu Kα (λ = 1.5406 Å). GSAS2 + EXPGUI software was used for Rietveld refinements. The content of Na, Ni, Mn and Li in P2-type NLNMO and O2-type LLNMO were tested by Inductively Coupled Plasma (ICP, M90, Bruker). X-ray photoelectron spectroscopy (XPS) tests were tested by a Thermo Fisher Scientific Model Kα spectrometer with Al

Kα radiation (1486.6 eV). The surface was bombarded in situ by Ar^+ ions accelerated to 1 keV for 0-120 s. The relevant high-resolution core line spectra (O 1s) of the bombarded surface were repeatedly collected 3 times. The measured data were fitted to the Gaussian peak shape with the Shirley type baseline. For in-situ XRD and Raman, the details including devices and measurement conditions will be introduced in in section 2.1.5 and 2.1.5, respectively. In-situ Differential Electrochemical Mass Spectrometry (DEMS) test was employed in in-situ Raman cell, which connected to the device of Perkin-Elmer (Clarus 680 and SQ 8S). The mass spectrometer is sensitive with oxygen molecular. The Mn K-edge and Ni L-edge of hard X-ray absorption spectroscopy (XAS) tests were employed at 10-ID beamline of APS at Argonne National Laboratory. The data were tested under fluorescence mode (I_f/I_0) and transmission mode ($\ln(I_0/I_t)$). The reference was measured under the transmission mode ($\ln(I_t/I_f)$). The energy scale of the spectra was calibrated with Sr_2RuO_4 and MnO reference measured simultaneously. Besides, all charged/discharged samples were prepared as free-standing electrodes with current collector of stainless steel.

2.1.4 Electrochemical tests

The 2032 coin-cell was used for electrochemical tests. The P2-type NLNMO and O2-type LLNMO electrodes were prepared by 70 % active material, 20 % acetylene black, and 10 % polytetrafluoroethene binder. The current collector for cathode is aluminum mesh (100 mesh). Typical loading of cathode active materials was around 5 mg cm^{-2}. Commercial 1 M $LiClO_4$/propylene carbonate (Tomiyama Pure Chemical Industries, LTD.) were employed as electrolyte and glass fiber was employed as separator. The lithium foil was employed as anode both in P2-type NLNMO and O2-type LLNMO half-cells. Besides, Na half-cell of NLNMO use the commercial 1 M $NaClO_4$ in propylene carbonate (Tomiyama Pure Chemical Industries, LTD.) as electrolyte and sodium foil as anode. The galvanostatic charge/discharge measurement was employed in Hokuto Denko HJ1001SD8 batteries stations.

2.1.5 In-situ XRD measurement

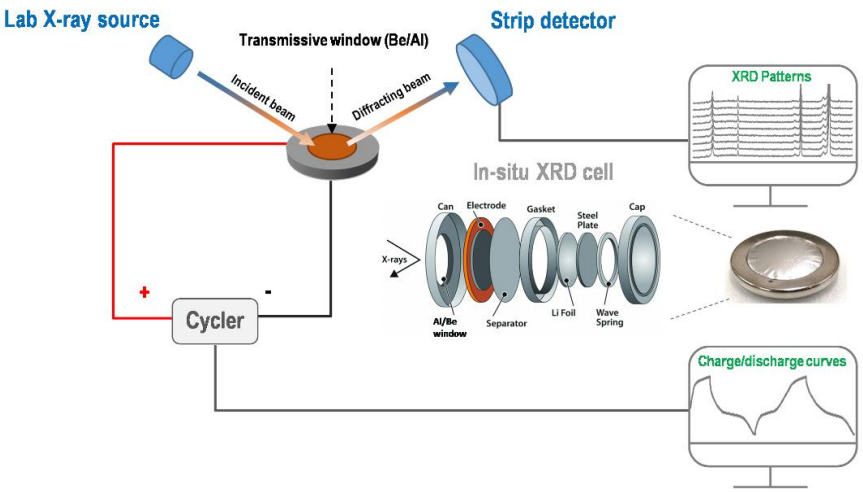

Figure 2. 1 The schematic diagram of in-situ XRD measurement. The schematic diagram of structural composition of in-situ XRD cell is from www.google.co.jp.

As shown in **Figure 2.1**, in-situ XRD measurement system consists of two parts. The first is experimental part, which contains X-ray system and in-situ XRD cell. The X-ray system consists lab X-ray source with Cu Kα and strip detector, which provides the incident X-ray and collects the XRD data during testing, respectively. The data of in-situ XRD patterns were tested from 15 ° to 60 ° with the 1.5 h and an interval of 3 min. The in-situ cell used the home-made cell, which is similar with 2032 cion cell. It includes the cathode can with Al/Be window, cathode electrode, separator, gasket, Li foil as anode, steel plate as current collector, wave spring and anode cap. The X-ray can pass through the Al/Be window and reach the electrode and reflect signals to collector. The corresponding image of in-situ XRD cell is shown. The second part contains the collector of XRD patterns and charge/discharge station. The collector can provide XRD patterns of electrode upon cycling, which displays the information of the phase transition and structure evolution upon charging and discharging. The charge/discharge station provides current for in-situ XRD cell, which allows the cell was measured for XRD and charge-discharge test at the same time. During the test in this chapter, the current density was 20 mA g^{-1}. Therefore, the results of in-situ XRD pattern and charge-discharge curve can be obtained meanwhile.

2.1.6 In-situ Raman measurement

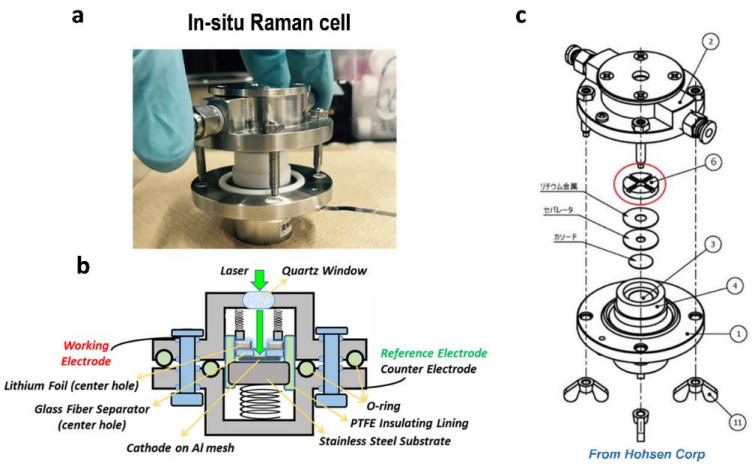

Figure 2. 2 a) Optical image of in-situ Raman device. b) The schematic diagram of in-situ Raman device. c) The components of the in-situ Raman device. The product was purchased from a company (Hohsen Corp., Osaka, Japan).

The in-situ Raman test collect the in-situ Raman spectra and charge-discharge profiles at the same time. The schematic diagram and image of in-situ Raman device are displayed in **Figure 2.2**. The in-situ cell has quartz window, which allows the laser to focus on the electrode. Furthermore, the spectra of the cathodes collected and collected by JASCO microscope spectrometer (NRS-1000DT). During cycling, in-situ Raman spectra can provide the information of oxygen behaviors such as peroxo and speroxo species. Meanwhile, the electrochemical station provides the charge/discharge profiles by galvanostatic test. Therefore, the results of Raman spectra and charge-discharge profiles can be obtained at the same time.

2.1.7 Highlights of Chapter 3

Utilizing anionic redox reactions has been considered as an effective method to obtain high-energy-density Li-ion battery systems because several Li-rich/excess cathodes break through the capacity limitation based on traditional TM redox reactions. However, the oxygen oxidation reactions are typically accompanied by irreversible gaseous oxygen release, which further accelerates irreversible TM migration to the AM

layer, resulting in harmful phase transition, which induced the durative voltage decay and serious capacity loss. By means of the novel O2-type structure, the electrode displays high specific capacity and structural stability compared with O3-type analogue obtained by solid-state reaction. The O2-type phase possesses oxygen stacking arrangement of ABAC with excellent structural stability, whereas O3-type structure with oxygen stacking arrangement of ABCABC converts to spinel phase upon cycling. The solid structure stability benefits from that the TM migration in AM layer was restrained, which suppresses the phase transition. Herein, by means of the novel structure, we focus on developing Li-rich/excess cathodes with O2-type structure by chemical/electrochemical ion exchange strategy to resolve the disadvantages of O3-type Li-rich/excess cathode materials. Moreover, it is significant to elucidate the charge compensation mechanisms by quantifying the capacity contributions of anionic and cationic redox reactions, which is beneficial for practical applications of oxygen redox chemistry.

2.2 Experimental section of Chapter 4

2.2.1 Synthesis of $Na_{0.6}Li_{0.2}Mn_{0.8}O_2$

$Na_{0.6}Li_{0.2}Mn_{0.8}O_2$ cathode material was prepared by solid-state reactions form Na_2CO_3, Li_2CO_3 and MnO_2 of stoichiometric amounts with an excess of 2 mol % Li_2CO_3 and Na_2CO_3 that were ball milled altogether for 24 h at the speed of 350 rpm. Moreover, the mixed powder was pelleted under the pressure of 2 MPa. Furthermore, it was calcined at 700 °C for 20 h in air. After quenching, the Na-deficient precursor $Na_{0.6}Li_{0.2}Mn_{0.8}O_2$ was stored in the glove box to further ion exchange and electrode preparation. All raw materials are purchased from the Wako company.

2.2.2 Synthesis of LMO

LMO was prepared by facile ion exchange strategy from $Na_{0.6}[Li_{0.2}Mn_{0.8}]O_2$ in molten salt. Firstly, the $Na_{0.6}[Li_{0.2}Mn_{0.8}]O_2$ and 10 times Li excess molten salts (88 % $LiNO_3$ and 12 % LiCl with mol ratio) milled altogether for 1 h. Then, the mixture put

into furnace and the reaction was operated at 280 °C for 1 h in air. After alternative ion exchange with equivalent Li, LMO can be obtained after washing with distilled water and dried at 90 °C for 15 h. All raw materials are purchased from the Wako company.

2.2.3 Synthesis of Li_2MnO_3

Li_2MnO_3 was prepared by solid-state reactions of $LiOH{\cdot}H_2O$ and $MnCO_3$. The ratio of between $LiOH{\cdot}H_2O$ and $MnCO_3$ is 2.1. The powders were mixed by using ball milling. The 10 mol % excess Li_2CO_3 was employed to compensate the Li loss. The mixed powder was calcined at 700 °C for 24 h in air.

2.2.4 Characterizations

The structure of the Na-deficient precursor $Na_{0.6}[Li_{0.2}Mn_{0.8}]O_2$ and LMO were investigated by XRD radiation with Cu Kα. GSAS2 + EXPGUI software was used for Rietveld refinement. The morphology was tested with SU8020 field emission scanning electron microscopy (FESEM). Both TEM and high-resolution transmission electron microscopy (HRTEM) were used JEM-200c microscope measured at 200 kV. The content of Na, Mn and Li in $Na_{0.6}[Li_{0.2}Mn_{0.8}]O_2$ and LMO_s were tested by ICP (M90, Bruker). For in-situ XRD and DEMS/Raman, the details including devices and measurement conditions will be introduced in in section 2.2.4 and 2.2.5, respectively. The O K-edge and Mn L-edge of soft XAS measurements were tested at 4-ID-C beamline of APS at Argonne National Laboratory. These measurements were tested under both the total electron yield (TEY) mode and total fluorescence yield (TFY) mode. The energy scale of the spectra was calibrated with these Sr_2RuO_4 and MnO reference measured simultaneously. Besides, all samples were prepared as electrodes with Al foil current collector and cycled at 10 mA/g. ^{7}Li Solid State Nuclear Magnetic Resonance (ssNMR) spectra were acquired by Bruker ASX200 spectrometer (4.7 T external magnetic field) at a Larmor frequency of −53.0 MHz.

2.2.3 Electrochemical tests

The 2032 coin-cell was employed for electrochemical tests. the Na-deficient precursor $Na_{0.6}Li_{0.2}Mn_{0.8}O_2$ and LMO as well as Li_2MnO_3 electrodes were prepared by 70 % active material, 20 % acetylene black, and 10 % polytetrafluoroethene binder. 1 M $LiClO_4$/$NaClO_4$ in propylene carbonate (PC) were used as electrolyte and glass fiber was employed as separator. The galvanostatic charge-discharge measurements were operated in Hokuto Denko HJ1001SD8 batteries stations.

2.2.4 In-situ XRD measurement

The in-situ XRD measurement is same with that in section 2.1.5. Both in-situ XRD cell and charge-discharge station are same with that used in section 2.1.5. During the test in this chapter, the current density was 10 mA g^{-1}. Therefore, the results of in-situ XRD data and charge-discharge profiles can be obtained meanwhile.

2.2.5 The combination of in-situ DEMS and Raman measurement

The schematic diagram and image of the in-situ DEMS/Raman system is displayed in **Figure 2.3**. The system contains three parts. The first part is in-situ DEMS test. The test used the in-situ Raman cell (from Hohsen Corp). It has intake and exhaust channel, which allows the Ar gas to enter and pass through the cell. During Li^+ (de)intercalation processes, it can collect the information of gases (O_2 and CO_2) generated by electrode and electrolyte. The device cell was performed for Raman, charge/discharge test and gas evolution meanwhile. The second part is in-situ Raman test, which is same with that in section 2.16. The final part is electrochemical station. The electrochemical station connects the in-situ cell and provides current for the cell. It provides the charge/discharge curves. During the test in this chapter, the current density was 10 mA g^{-1}. The three parts work at the same time. Therefore, the results of in-situ Raman spectra and gas evolution (O_2 and CO_2) as well as charge/discharge curves can be obtained at the same time during Li^+ (de)intercalation processes.

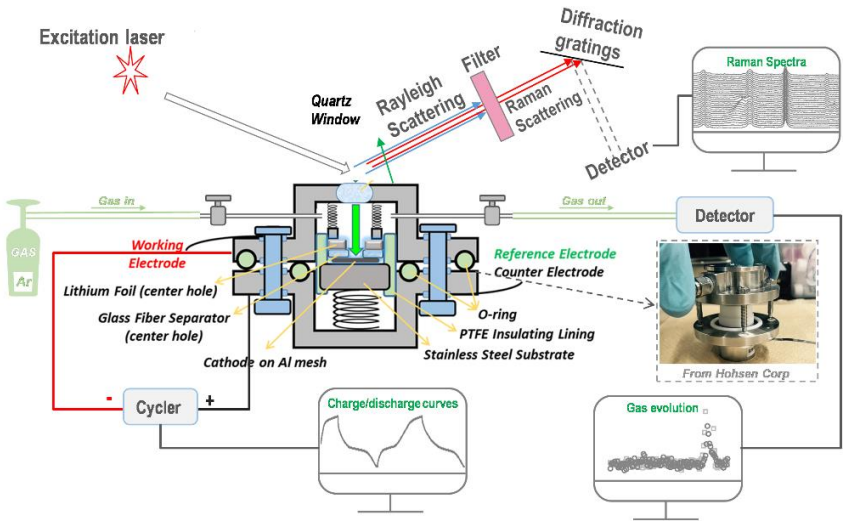

Figure 2. 3 The schematic of systems of the combination of in-situ DEMS/Raman measurement.

2.2.6 Highlights of Chapter 4

By means of oxygen redox chemistry, the available capacity of Li-rich cathode materials reaches higher value than theory capacity triggered by TM-based redox reactions. However, the serious irreversible capacity upon initial cycle was ascribed to excessive oxidation. The final product is oxygen molecule, which is hard to be reversibly reduced during discharging. Moreover, it would induce the serious capacity loss. Furthermore, the gaseous oxygen loss accelerates harmful layered/spinel phase transition induced by irreversible TM migration. It causes the further structural distortion and electrochemical decay during long-term cycling. Thus, it is important to explore more modification strategies to restrain oxygen loss upon the initial oxygen activation process. Besides, the complex anionic/cationic redox reactions are also not beneficial for clarifying the charge compensation mechanisms. Herein, we designed a unique O3-type Li-excess layered cathode material, $Li_{0.6}[Li_{0.2}Mn_{0.8}]O_2$, with Li-deficient state while TM layer displays Li-excess state. By designing the Li ration in AM layer, during the subsequent initial discharging, the oxidized lattice oxygen can be effectively reduced to lattice oxygen. Besides, by using spectroscopic characterizations, the charge compensation mechanism of complex Mn-based and O-related redox reactions can be clearly clarified during charging and discharging processes.

Chapter 3. Achieving stable cationic and anionic redox reactions in Li-excess O2-type layered cathode by chemical ion exchange strategy

3.1 Introduction

Utilizing anionic redox reactions is an effective method to obtain high-energy-density Li-ion batteries because several Li-rich/excess cathodes with have broken the traditional capacity bottleneck.[51] However, the oxygen oxidation reactions are typically accompanied by irreversible gaseous oxygen release, which further accelerates irreversible TM migration, resulting in harmful layered/spinel phase transition, which causes durative voltage decay and serious capacity loss.[52]

Ion exchange strategy is useful for exploring inorganic materials with novel structures because the final products would inherit main crystal frameworks from their parent phases and harvest various improved physical and chemistry features.[53] For Li-ion battery electrode materials, the ion exchange strategy has been used frequently for designing and preparing layered oxide materials with novel structures.[54-55] The routes of ion exchange strategy include chemical methods within various media and electrochemical approaches.[56-58] In detail, via Li^+/Na^+ ion exchange, the Li compounds would possess new coordination environments of Li and oxygen stacking arrangements, which is impossible for materials obtained by traditional solid-state reactions. The new structures might own some beneficial structural stability and electrochemical performances.[59] For example, Paulsen et al. prepared O2-type $Li_{2/3}Ni_{1/3}Mn_{2/3}O_2$ via Li^+/Na^+ ion exchange method.[60] By means of the novel O2-type structure, the electrode displays high specific capacity and structural stability compared with O3-type $LiNi_{1/2}Mn_{1/2}O_2$ obtained by solid-state reactions. The O2-type structure possesses oxygen stacking arrangement of ABAC, which is beneficial for structural stability, whereas O3-type phase with oxygen stacking arrangement of ABCABC converts to spinel phase upon cycling.[55] The solid structure stability benefits from that TM

migration in AM layer was restrained, which inhibits the spinel phase transition.[48] Herein, we focus on developing the Li-rich/excess cathodes with O2-type structure by chemical/electrochemical ion exchange strategy to resolve the disadvantages of O3-type materials. Moreover, the charge compensation mechanism should be unraveled by quantifying the capacity contributions of anionic and cationic redox reactions, which is beneficial for practical applications.

We developed O2-type LLNMO by the optimal chemical Li^+/Na^+ ion exchange procedure from P2-type NLNMO. Within LLNMO electrode, the phase transition and irreversible oxygen release can be well restrained, displaying the excellent structural and electrochemical stability. As a comparison, a similar O2-type oxide obtained via electrochemical ion exchange displayed serious oxygen release and voltage decay. We demonstrate that chemical ion exchange is beneficial for obtaining stable structure and pure phase from the aspect of methodology. On the other hand, the LLNMO have reversible anionic/cationic redox reactions, which was clearly quantified, clarifying the underlying charge compensation mechanisms.

3.2 Structural and electrochemical characterizations of NLNMO and LLNMO

3.2.1 Structural and electrochemical characterizations of NLNMO

The Na-based precursor $Na_{0.66}[Li_{0.12}Ni_{0.15}Mn_{0.73}]O_2$ (defined as NLNMO) was synthesized by traditional solid state reactions at high temperature. The details were shown in experiment section 2.1.1. The Rietveld refinement of XRD and ICP tests were used to obtain the detailed lattice parameters and chemical composition. As shown in **Figure 3.1a** and **Table 3.1**, the calculated pattern obtained from the software of GSAS2 fits well with the experimental pattern, which provides the precise fitting results with low error of R_{wp}=4.71 %, χ^2 = 1.46. It proved that the structure of NLNMO was accurately indexed as P2-type structure with *$P6_3/mmc$* space group. The refined parameters were a = b = 2.8752(6) Å, c = 11.1761(6) Å, V = 80.016 $Å^3$, α = β = 90°

and γ = 120°. The P2-type NLNMO also exhibits ABBA oxygen stacking arrangement, which is shown in **Figure 3.1a** insert. Besides, the composition was confirmed by ICP, delivering the chemical formula of $Na_{0.66}[Li_{0.12}Ni_{0.15}Mn_{0.73}]O_2$. Therefore, the NLNMO can be demonstrated as a P2-type layered oxide, which is derived from P2-type $Na_{2/3}MnO_2$, where partial $Mn^{3+/4+}$ were replaced by Li^+/Ni^{2+}.[61] Owing to the absence of superlattice peaks in range of 20°–30°, the Li, Ni and Mn in TM layer irregularly occupy the octahedral sites, while all of Na^+ ions within AM layer occupy the trigonal prismatic sites.[62]

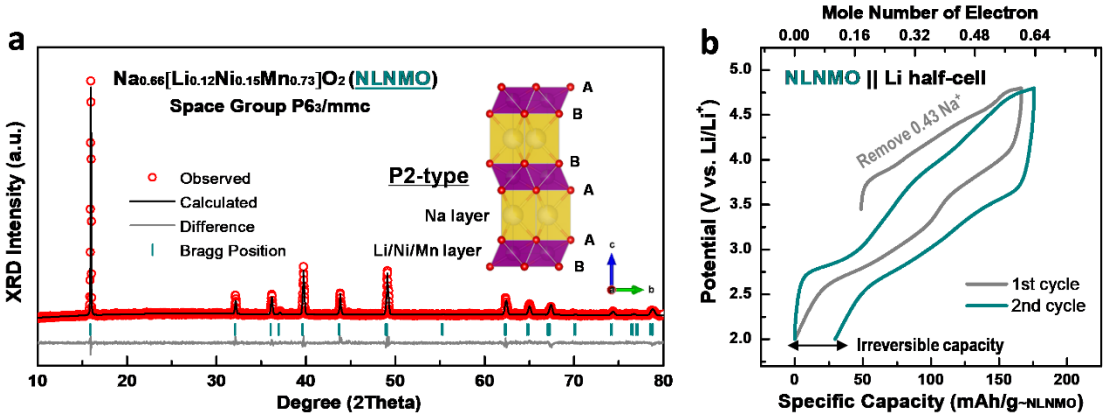

Figure 3. 1 a) The XRD pattern of P2-type NLNMO. b) The charge/discharge curves of NLNMO in Li-half cell.

To achieve the electrochemical ion exchange process, the NLNMO electrode was assembled in Li half-cell, in which the Na-based NLNMO as cathode and Li metal as anode, which is shown in **Figure 3.1b**. During the first charging, the NLNMO displays a sloping voltage profile, where the charge capacity can be attributed by the 0.43 mol Na^+ removal. After Na^+ deintercalation process, the first discharge process could be regarded as the Li^+ dominated intercalation process because Li half-cell provides the high concentration of Li^+ ions from both electrolyte and Li-metal anode. Furthermore, NLNMO electrode displays the typical "S-shape" profiles during second cycle, which is like with that of LLNMO. After several Li^+ deintercalation processes, Na^+ ions in NLNMO can be gradually replaced by the Li^+ ions as dominated charge carrier. Nonetheless, it is possible that a small quantity of Na^+ ions would still reinsert into

or/and stay at AM layer during this process. Besides, the NLNMO electrode displays the discharge capacity of 166 and 146 mAh g^{-1} upon first and second cycles, respectively.

Table 3. 1 Refined lattice parameters obtained by XRD Rietveld refinement for NLNMO. S.G. *P6₃/mmc*, a = b = 2.8752(6) Å, c = 11.1761(6) Å, V = 80.016 Å^3, α = β = 90°, γ = 120°, Rwp=4.71 %, χ2 = 1.46.

Atom	Site	x	y	z	Occ	Uiso
Mn1	2a	0	0	0	0.73	0.02274
Ni1	2a	0	0	0	0.15	0.00896
Li1	3a	0	0	0	0.12	0.02344
Na1	2b	0	0	0.25	0.3333	0.18061
Na2	2d	0.3333	0.6667	0.75	0.3272	0.05048
O1	4f	0.3333	0.6667	0.08121	1	0.08474

Table 3. 2 Stoichiometry from ICP results of NLNMO.

elements	content (mg/L)	mol ratio	valence
Na	2.51	0.66	+1
Li	0.14	0.12	+1
Mn	6.65	0.72	+4
Ni	1.46	0.14	+2

3.2.2 Structural and electrochemical characterizations of LLNMO

The O2-type layered $Li_{0.66}[Li_{0.12}Ni_{0.15}Mn_{0.73}]O_2$ (defined as LLNMO) was prepared by chemical ion exchange from NLNMO. The details were shown in experiment section 2.1.2. The Rietveld refinement of XRD was used to obtain the detailed lattice parameters. As shown in **Figure 3.2a** and **Table 3.3**, the calculated pattern obtained from the GSAS2 fits well with experiment pattern, which provides the precise fitting results with low error of R_{wp}=4.93 %, χ^2 = 1.79. It proves that the structure of LLNMO can be accurately indexed as the hexagonal O2-type structure with *P6₃mc* space

group.[63] The refined parameters were a = b = 2.8375(9) Å, c = 9.6564(1) Å, V = 67.336 Å^3, α = β = 90° and γ = 120°. The O2-type LLNMO also exhibits ABAC oxygen stacking arrangement, which is shown in **Figure 3.2a** insert. Besides, the ICP result in **Table 3.4** proves that the chemical ion exchange strategy can achieve the almost complete Li^+/Na^+ exchange within AM layer. The chemical formula of LLNMO also can be confirmed regardless of a trace amount of Na^+ ions residue.[59] The LLNMO is derived from O2-type $Li_{2/3}Ni_{1/3}Mn_{2/3}O_2$.[55] Compared with XRD pattern of NLNMO, the location of (002) peak shifts to higher diffraction angle, which suggests the decreasing of interlayer distance.[64] It caused by the obvious change of coordination environment during Li^+/Na^+ exchange process, which also induce the P2/O2 phase transition because Li prefers occupies octahedral site, while Na has both prismatic and octahedral locations. Besides, the evolution of oxygen stacking rearrangement from ABBA (P2-type) to ABAC (O2-type) during ion exchange process is caused by the gliding of TM layers.[65-66]

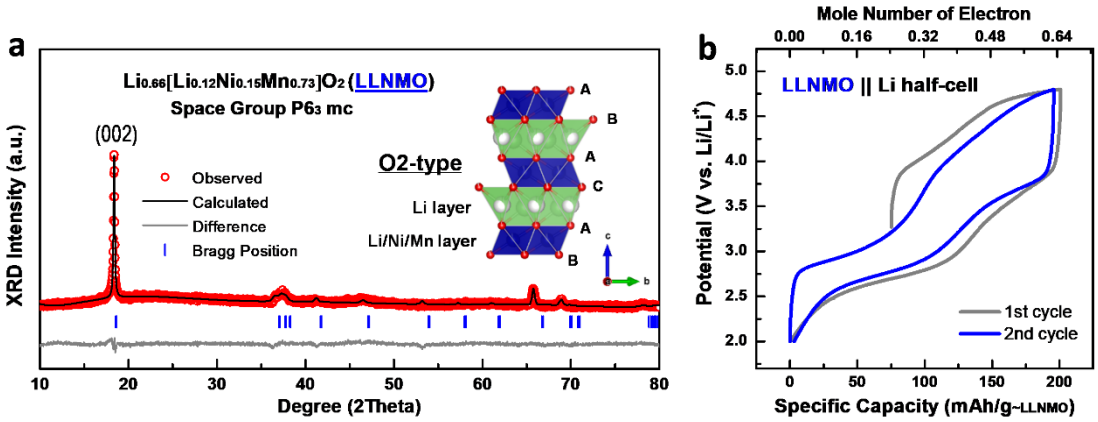

Figure 3. 2 a) The XRD pattern of O2-type LLNMO at pristine state. b) The charge/discharge curves of LLNMO in Li-half cell.

The LLNMO electrode was also tested in Li half-cell with galvanostatic charge/discharge test. The second discharge curve is like that of the first discharge in LLNMO, whereas the obvious voltage decay was caught within NLNMO during the second cycle. Moreover, LLNMO delivered the limited irreversible capacity of 2.9 mAh g^{-1} during the second discharging. On the contrary, an obvious irreversible

capacity of 30 mAh g^{-1} was measured in NLNMO, which suggests more reversible electrochemical reactions exist within LLNMO electrode. Besides, the NLNMO electrode displayed the capacity of 201 and 196 mAh g^{-1} upon the first and second cycles, respectively. Therefore, it is not hard to find that the stable and reversible electrochemical behaviors can be achieved by chemical ion exchange strategy.

Table 3. 3 Refined crystallographic parameters by XRD Rietveld refinement for LLNMO. S.G. *P6₃mc*, a = b = 2.8375(9) Å, c = 9.6564(1) Å, V = 67.336 Å^3, α = β = 90°, γ = 120°, Rwp=4.93 %, χ2 = 1.79.

Atom	Site	x	y	z	Occ	Uiso
Mn1	2a	0.6667	0.3333	0	0.73	0.02025
Ni1	2a	0.6667	0.3333	0	0.15	0.01649
Li1	3a	0.6667	0.3333	0	0.12	0.01558
Li2	2b	0.3333	0.6667	0.2412	0.66	0.01142
O1	4f	0.3333	0.6667	0.50258	1	0.10885

Table 3. 4 Stoichiometry from ICP results of LLNMO.

elements	content (mg/L)	mol ratio	valence
Na	0.04	0.01	+1
Li	0.73	0.78	+1
Mn	5.44	0.73	+4
Ni	1.20	0.15	+2

3.3 Structural and phase evolution processes of NLNMO and LLNMO

As shown in **Figure 3.3**, the 2nd-10th normalized discharge curves of both NLNMO and LLNMO were performed to clearly show the voltage retention, which is relevant with the phase transition in layered structures. Under the same electrochemical condition, only the slight voltage decay can be shown in LLNMO electrode, whereas NLNMO electrode displays the severe fade of output voltage during the initial 10 cycles.

The phenomenon suggests that the structural change such as layered/spinel phase transition have occurred in the NLNMO electrode. Next, we would use ex-situ XRD, Raman and in-situ DEMS characterizations to prove the speculation.

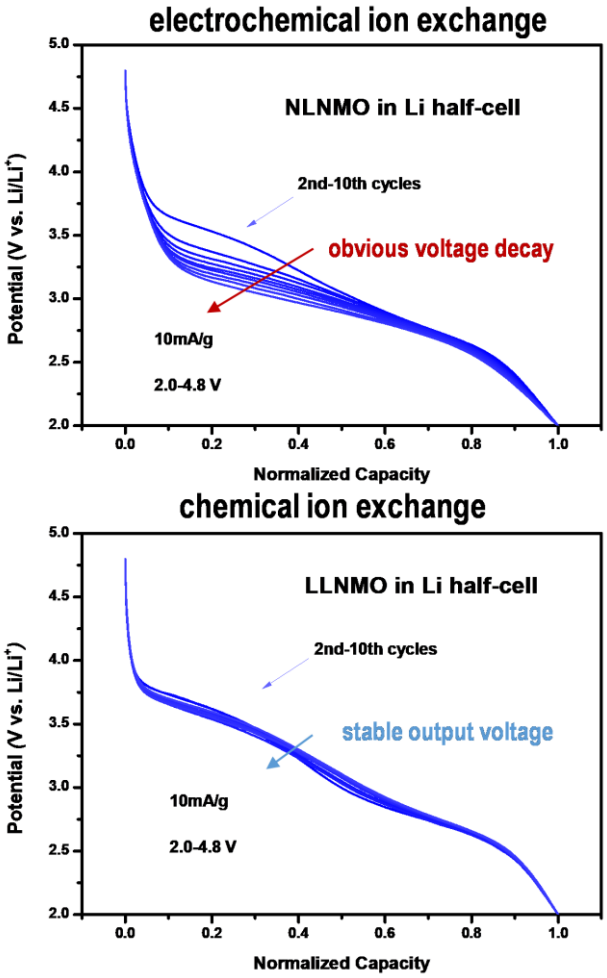

Figure 3. 3 The 2nd-10th normalized discharge curves of a) NLNMO and b) LLNMO within Li half-cells.

The ex-situ XRD measurements were used for studying the structure evolution within NLNMO and LLNMO, which is shown in **Figure 3.4**. Both NLNMO and LLNMO electrode are tested in Li half-cell and remove these cathodes at second discharged state. In comparison with the pristine XRD pattern of NLNMO electrode in **Figure 3.1a**, the location of (002) peak shifted to higher angle after two cycles. Meanwhile, the signals of P2-type phase were disappeared, which is caused by the Li^+ inserted the AM layer during electrochemical ion exchange. The XRD refinement proves the P2/O2 phase transition occurred, demonstrating the Li^+ becomes the

dominated charge carrier after two cycles.[67] Notably, a small peak located at around 16° can be detected, which corresponds to a trace amount of Na-based P2 phase because of residual Na^+ ions in AM layer.[59] The subsequent voltage decay during initial 10 cycles might be contributed by the incomplete phase transition. It further causes the structure distortion such as the formation of spinel phase. Therefore, the electrochemical ion exchange is not beneficial for the electrochemical performance. On the contrary, the O2-type structure with absence of impurities can be well detected in LLNMO electrode. It provided the solid foundation for structure stability. In a word, the structural stability of O2-type LLNMO generated via chemical ion exchange strategy is superior to the counterpart obtained by electrochemical ion exchange process.

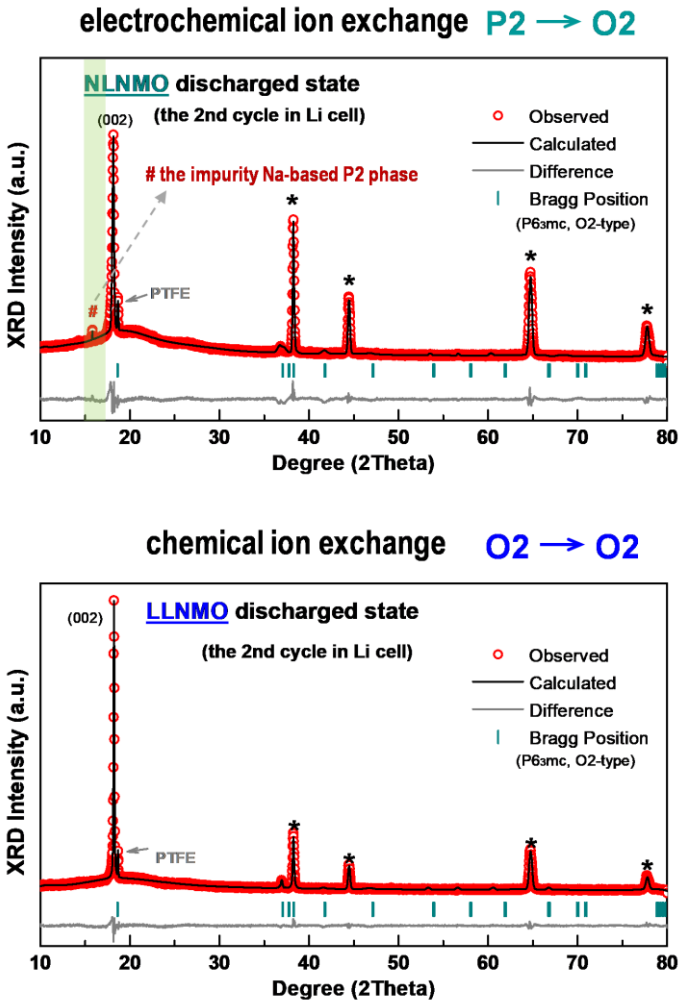

Figure 3. 4 The ex-situ XRD patterns of a) NLNMO and b) LLNMO electrodes after two cycles in Li half-cells.

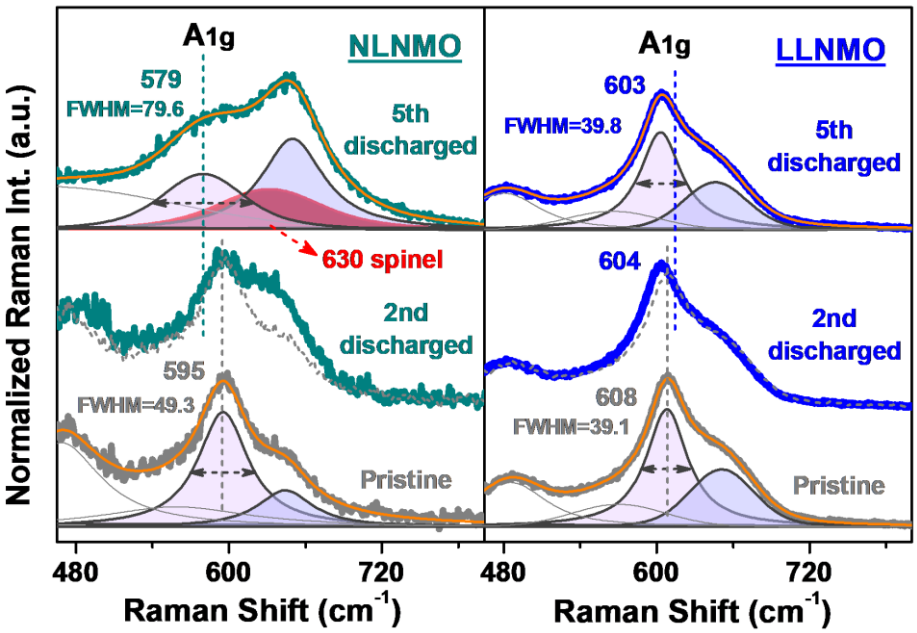

Figure 3. 5 The ex-situ Raman spectra of NLNMO and LLNMO electrodes. The samples were collected at pristine state and after the 2nd and 5th cycles.

To unravel the underlying reasons for the electrochemical performance difference between NLNMO and LLNMO electrode, ex-situ Raman measurement was performed in **Figure 3.5**. Compared with pristine NLNMO electrode, the Raman spectrum of second discharged electrode displayed a similar location of main peak at around 595 cm^{-1}, which corresponds to symmetric A_{1g} mode.[68] However, the second discharged sample also exhibited a wide shoulder located at around 630 cm^{-1}, reflecting the structural rearrangement occurred in NLNMO.[69] Moreover, the Raman spectrum of 5^{th} discharged sample showed many obvious changes. At first, the position of main peak delivered a shift from 595 to 648 cm^{-1}. Secondly, the main peak occurred a pronounced broadening, which suggests the formation of spinel phase located at around 630 cm^{-1}.[70] At last, the peak of the A_{1g} mode corresponding to TM-O stretching showed a visual broadening, which was caused by the cationic ion mixing or/and the faults of oxygen stacking during initial 5 cycles.[71] Besides, the peak located at around 480 cm^{-1} almost disappeared after 5 cycles, which was ascribed to irreversible TM migration. The irreversible TM migration would cause the unfavorable phase transition, which is harmful for electrochemical performance. These Raman spectra suggest that

the layered NLNMO at pristine state partially converts to a spinel structure during initial 5 cycles, which can explain the reason of the voltage decay.[71] On the contrary, for LLNMO electrode during 5 cycles, the spectrum of both 2nd and 5th discharged sample shows similar position and full width at-half maximum of A_{1g} to that of pristine state, demonstrating the layered structure of LLNMO can be well kept upon cycling.

3.4 Oxygen behaviors in NLNMO and LLNMO electrode

3.4.1 The in-situ DEMS of NLNMO and LLNMO electrodes

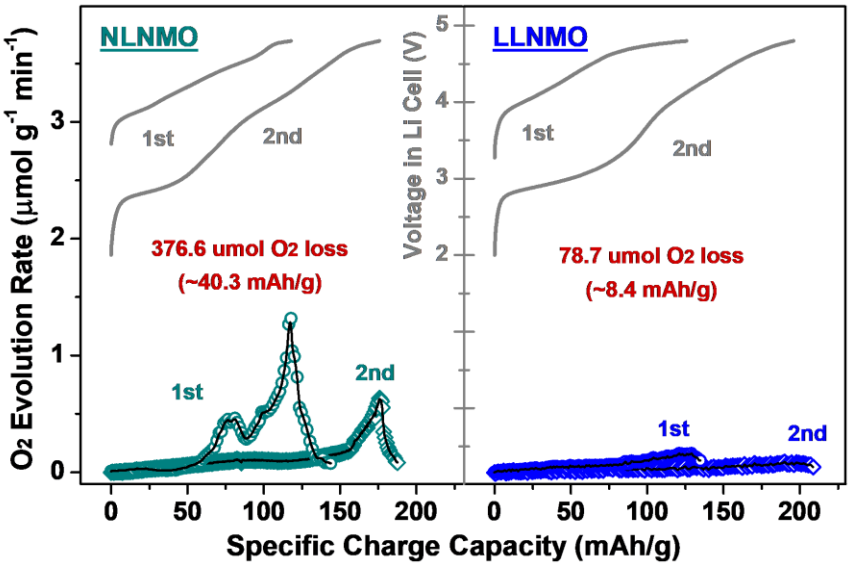

Figure 3. 6 In-situ DEMS of NLNMO and LLNMO electrodes upon the first two charging processes.

To clarify the underlying reason for the electrochemical reversibility, in-situ DEMS was employed to investigate the oxygen evolution of NLNMO and LLNMO electrode in **Figure 3.6**. For NLNMO electrode, severe O_2 release can be obviously observed up first charging. The oxygen release was calculated as the 376.6 μmol, which is based on the active material in cathode. The formation of gaseous oxygen only came from the oxidation reaction from lattice oxygen instead of electrolyte degradation. Moreover, the gaseous oxygen evolution from O^{2-} is based on $4e^-$ reaction.[43] Thus, the irreversible capacity is 40.3 mAh g^{-1} contributed by excess oxygen oxidation. However, the slight oxygen loss of 78.7 μmol and irreversible capacity of 8.4 mAh g^{-1} can be achieved,

which is consistent with the slight irreversible capacity upon initial two cycles. Upon second charging, the destructive oxygen release can be effectively restrained within LLNMO electrode, whereas NLNMO electrode suffered from the serious oxygen loss at the end of second charging. Therefore, the stable and reversible anionic redox reactions were achieved in O2-type layered LLNMO.

3.4.2 The in-situ Raman of NLNMO and LLNMO electrodes

As shown in **Figure 3.7**, in-situ Raman measurement was performed to study oxygen behaviors in NLNMO and LLNMO electrodes. Compared with pristine LLNMO, a newly peak located at the range from 795 to 845 cm^{-1} was ascribed to the peroxo species upon the first charging. Besides, the blue shift of the new peak was attributed to the decreasing of O–O distance during Li^+ deintercalation process.[72] During the subsequent discharge, the signal of peroxo-like can be still observed and the intensity gradually decreased in this region, which proves the oxidized lattice oxygen species were gradually reduced upon this process. Until discharged to 2.0 V, the signal disappeared, suggesting the oxidized lattice oxygen species have been fully reduced at the ending of initial discharge process. Even to the second cycle, the single of oxidized lattice oxygen displays a reversible evolution both in intensity and peak position. These results further demonstrated the oxygen redox reactions were reversible within LLNMO electrode. Likewise, for NLNMO electrode tested in Li metal half-cell, the Raman spectra at charged states also detected the signal of peroxo-related during initial charging, which confirms the existence of oxygen oxidation reactions in NLNMO. Notably, an obvious peak located at around 1104 cm^{-1} can be detected upon the initial charging, which is ascribed as the appearance of superoxo species (O_2^-).[73] The O_2^- is easily to be further oxidized to oxygen molecule (O_2), which induces the serious oxygen release upon oxygen activation process. The results of in-situ Raman spectra of NLNMO are consist with the observations in DEMS part. Although the LLNMO was obtained from NLNMO by chemical ion exchange, the signal of superoxo species cannot be observed during initial two cycles. Therefore, in-situ Raman measurement

also demonstrate that the reversibility of oxygen redox reactions in O2-type LLNMO is superior than O2-type Li-excess oxide obtained by electrochemical ion exchange route.

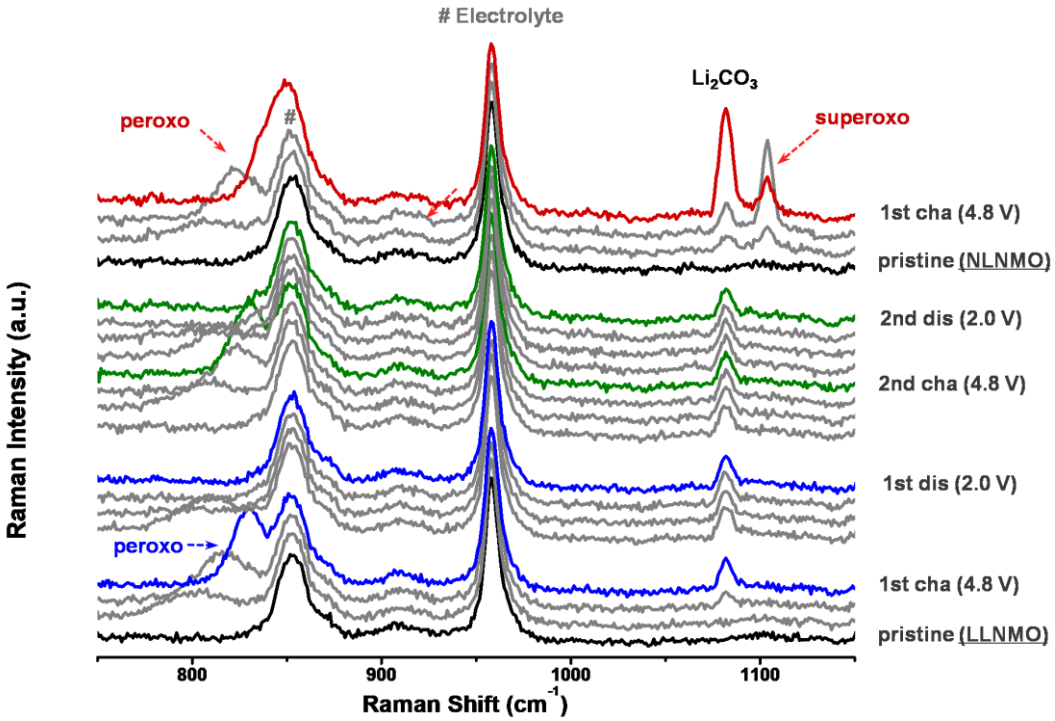

Figure 3. 7 In-situ Raman spectra of LLNMO and NLNMO.

3.5 Analysis of cationic/anionic redox reactions in LLNMO

3.5.1 XPS and hard XAS spectra of LLNMO

As the optimized O2-type electrode, LLNMO was selected to further investigate the detailed oxygen-related activities by XPS. As shown in **Figure 3.8**, at pristine state, the peak of lattice oxygen (O^{2-}) in O 1s XPS was located at 529.3 eV. Moreover, the peaks located at 531.1 and 532.8 eV can be ascribed to the oxygenated deposited species of C=O and C–O, respectively.[74] After the first charge, an obvious signal of oxidized lattice oxygen (O^{n-}) appeared at around 530.8 eV, which indicates oxygen-related activities have been triggered upon initial charging.[75] Until discharged to 3.0 V, the signal of O^{n-} peak was still visual. Furthermore, it disappeared after discharging to 2.0 V, suggesting O^{n-} species have been reduced to O^{2-} upon the first discharging.

Remarkably, the O^{n-} signal was detected again at the second charged state, which demonstrates a sustained participation of reversible oxygen redox reactions exists in LLNMO electrode. Besides, the use of Ar^{+} sputter etching can increase the probe depth from several nanometers to ≈100 nm, which is an effective method to detect bulk signal of oxygen-related activities. The fittings of 1st charged sample spectra with different prove depth provided the average relative ratios of O^{n-}, which is respect to the lattice oxygen component. With increasing the probe depth, the signal of O^{n-} can be continuously observed at the charged states without drastic decline in the value of relative amount of O^{n-}. These results demonstrated the reversible oxygen redox reactions can be detected on surface and in bulk material.

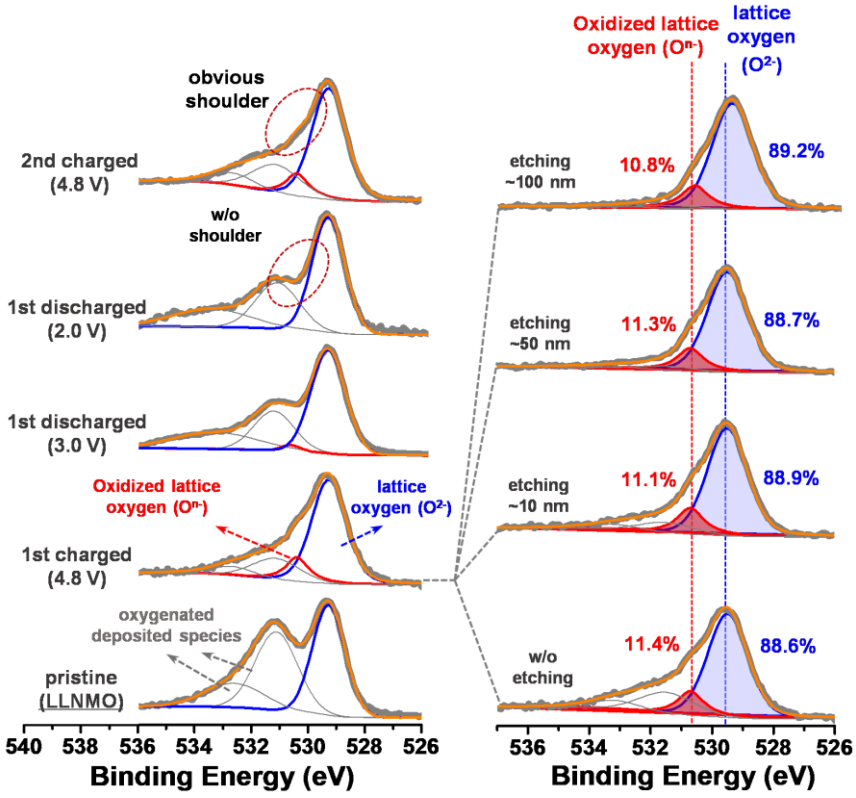

Figure 3. 8 The ex-situ O 1s XPS spectra of LLNMO tested at different charged/discharged states. And the O 1s XPS spectra of 1st charged LLNMO with various etching depths were also shown

After clarifying the charge compensation mechanisms based on oxygen redox reaction, hard XAS of Ni K-edge and Mn K-edge was employed to study the evolutions of Ni/Mn oxidation states.[76] As shown in **Figure 3.9**, the change in absorption edge

can guide the trend of oxidation states of Ni /Mn during charging and discharging. Herein, the enlarged rising edge and 1st derivative curves are shown to clearly derive the trend in absorption edge. In **Figure 3.9a**, the oxidation state of Ni in pristine LLNMO was +2, which was deduced from XRD and ICP results. After charging to 4.8 V, the spectrum of Ni K-edge shifted to high energy, suggesting the oxidation reactions of Ni^{2+} to $Ni^{3+/4+}$. Furthermore, the spectrum of Ni K-edge approximately shifted to pristine location when discharged to 3 V, which can be attributed to that most Ni ions with high oxidation state are reversibly reduced to Ni^{2+} during initial discharge process. Notably, when O2-LLNMO are discharged from 3 to 2 V, there is no significant evolution of Ni oxidation state, implying Ni redox reaction did not participated upon the discharging process. Moreover, after recharged to 4.8V, the Ni K-edge spectrum shifts to high photon energy again, which is similar to that of first charged state. Thus, it is rational to deduce that Ni redox reactions undergo reversible processes upon two cycles. In **Figure 3.9b**, for Mn-based redox reactions, the Mn valence with in pristine LLNMO was +4. Upon the initial charging, the edge position of Mn K-edge spectrum kept constant, displaying the Mn oxidation state was unchanged during this process. Notably, the Ni oxidation reactions cannot provide all of charge capacity, demonstrating the oxygen oxidation reactions provided the partial capacity upon the process, which is consistent with other Li-rich/excess materials. Upon the subsequent discharged to 3 V, Mn oxidation state remained +4, suggesting Mn-based redox reactions are not obviously related to this process. After discharged to 2.0 V, an obvious shift of absorption edge in Mn K-edge spectrum can be detected, whereas the Ni K-edge spectra did not shift in this low-voltage range. It is a common phenomenon that the partial manganese reduction occurs at the low voltage during discharging, which is consistent with previous studies observed in Ni/Mn-based Li-rich/excess oxide materials.[76] Therefore, the oxidation state of Mn kept constant in the voltage range from 3 to 4.8 V, whereas Mn was obviously reduced in voltage range from 3 to 2 V upon the initial discharging. After the second charged, the Mn oxidation state increased

to that at pristine state, suggesting Mn redox reactions delivered the reversible processes upon two cycles.

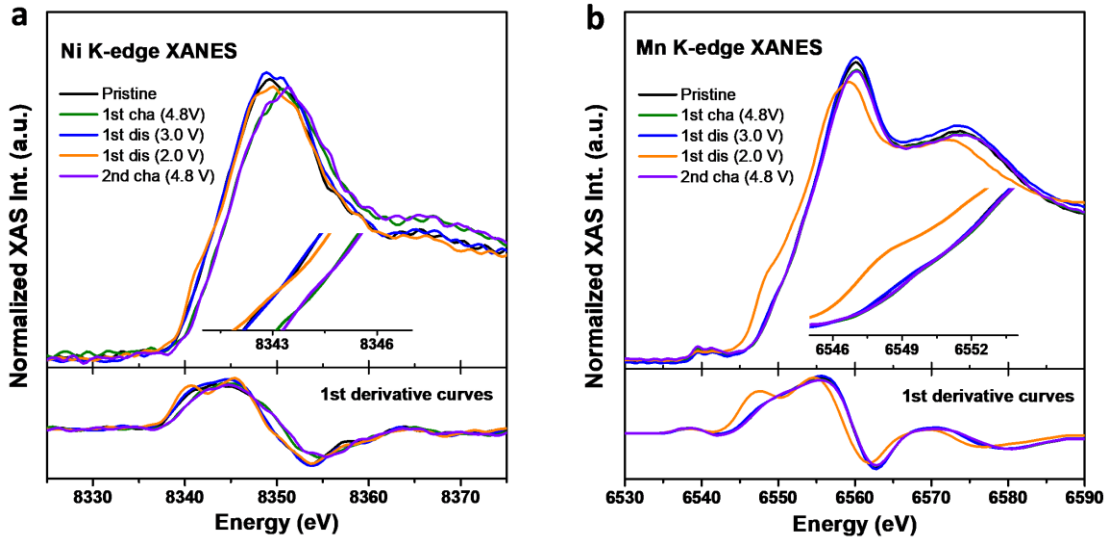

Figure 3. 9 The a) Ni K-edge and b) Mn K-edge XAS of LLNMO electrodes.

3.5.2 The capacity distributions of LLNMO during cycling

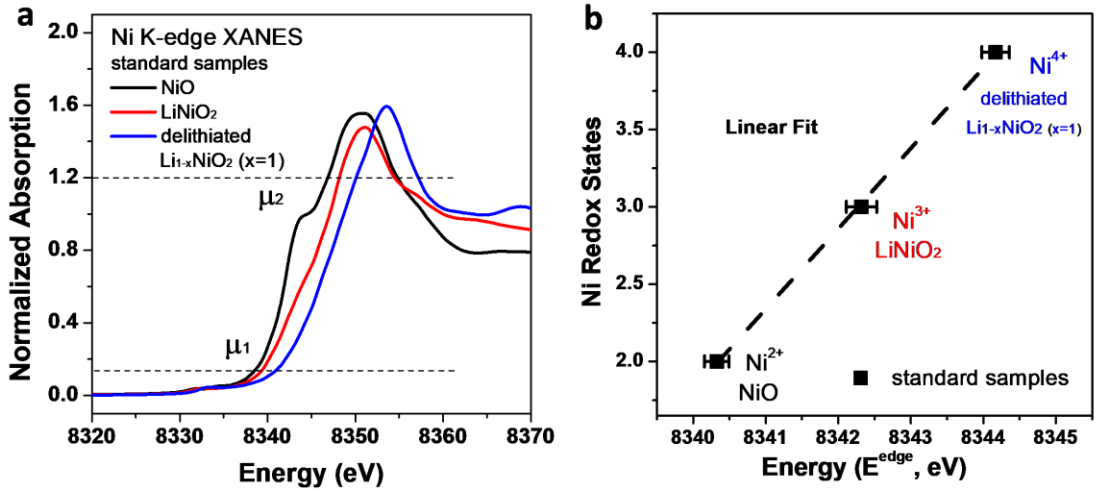

Figure 3. 10 a) a) The normalized Ni standard K-edge XAS spectra of Ni^{2+}, Ni^{3+} and Ni^{4+} reference samples. b) Linear relationship between the oxidation states of Ni and the K-edge positions.

Next, to better clarify the charge compensation mechanism, the specific capacity contributions of anionic/cationic redox reactions are evaluated at first. Herein, an integral method was employed to quantitatively determine the Ni/Mn oxidation state at different charged states.[77] At first, the integral method can build a linear relationship

between the oxidation states and edge positions, which is irrespective with edge shape of XAS spectra.

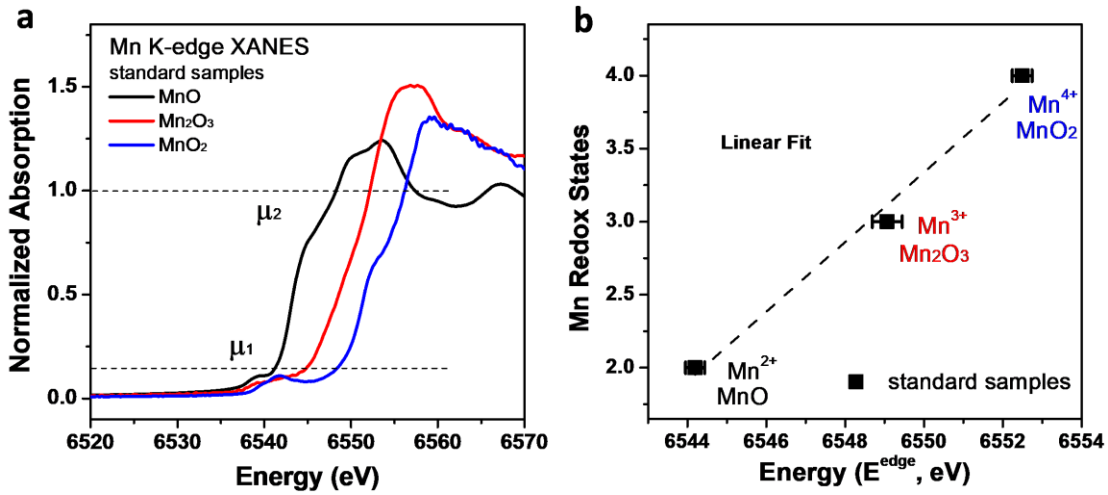

Figure 3. 11 a) The normalized Mn K-edge XAS spectra of MnO, Mn_2O_3 and MnO_2 reference samples. (b) Linear relationship between the oxidation states of Mn and the K-edge positions.

As shown in **Figure 3.10**, the NiO (Ni^{2+}), $LiNiO_2$ (Ni^{3+}) and delithiated $Li_{1-x}NiO_2$ (x=1, Ni^{4+}) are selected as reference samples to provide normalized Ni K-edge XANES spectra. Moreover, linear relationship between Ni oxidation state and K-edge position was determined by the integral method. Herein, all spectra of samples and references were normalized.[78] The integral method has been shown to provide excellent linear relationship between Ni oxidation states of standard samples and edge positions. Integration was carried out between $\mu_1 = 0.15$ and $\mu_2 = 1.2$ on each normalized spectrum to remove contributions from the pre-edge and account for changes of absorption edge shape, due to coordination environments, on the average edge energy. Therefore, Ni oxidation state of LLNMO at different charged/discharged states can be obtained from the linear relationship obtained from integral method.

As shown in **Figure 3.11**, MnO, Mn_2O_3 and MnO_2 were selected as reference samples to provide standard spectra of Mn K-edge XAS. The integral method has been shown to provide the linear relationship between Mn oxidation states of standard samples and edge positions. Integration was carried out between $\mu_1 = 0.15$ and $\mu_2 = 1.0$ on each normalized spectrum to remove contributions from the pre-edge and account

for changes of absorption edge shape, due to coordination environments, on the average edge energy. Therefore, Mn oxidation state at different charged states also can be obtained by integral method.

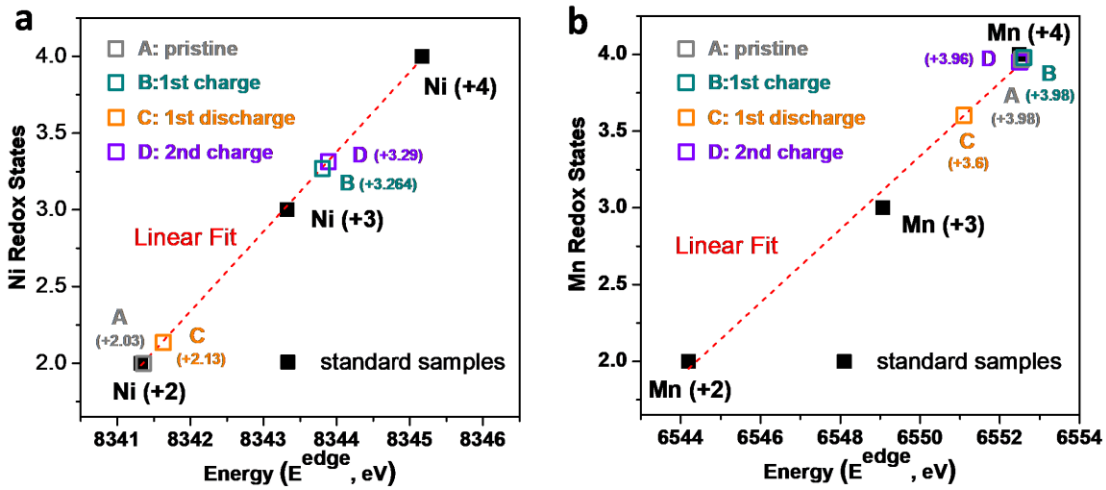

Figure 3. 12 A summary of the estimated oxidation states of a) Ni and b) Mn upon the first two cycles.

Furthermore, the estimated average Ni/Mn oxidation state within LLNMO electrode can be quantified, which is shown in **Figure 3.12**. According to the evolution of Ni/Mn oxidation state, the corresponding capacity can be calculated, which is summarized in **Figure 3.13**. Upon first charging, the Ni oxidation state of +2.03 in pristine sample increased to +3.26 at first charged state, delivering a charge capacity of ≈ 58.8 mAh g^{-1} triggered by Ni oxidation reaction. Meanwhile, the Mn oxidation state remained +3.98. Thus, anionic oxygen oxidation reactions deliver the charge capacity of ≈ 67.1 mAh g^{-1}. Furthermore, after discharged to 2 V, the capacity contributions of Ni/Mn reduction reactions were calculated as ≈ 52.9 and 90.5 mAh g^{-1}, respectively. Upon this discharging process, the oxygen reduction reactions obtained the reversible capacity of ≈ 57.1 mAh g^{-1}, delivering an irreversible capacity of ≈ 10 mAh g^{-1}. The DEMS results also proved the value was triggered by oxygen release. During the subsequent charging, the capacity contributions based on Ni, Mn and oxygen can be evaluated as ≈ 54.3, 82.7 and 58 mAh g^{-1}, respectively. Thus, we can estimate approximate average oxidation states of different charged samples and capacity contributions of Ni/Mn oxidation/reduction reactions during charge/discharge processes by using the integral

method. And then, the capacity distributions of oxygen redox reaction can be obtained by the differences between total electrochemical capacity and Ni and Mn capacity distributions. Thus, all capacity contributions of cationic/anionic redox reaction can be calculated. The results are useful for clarifying the complex charge compensation mechanisms.

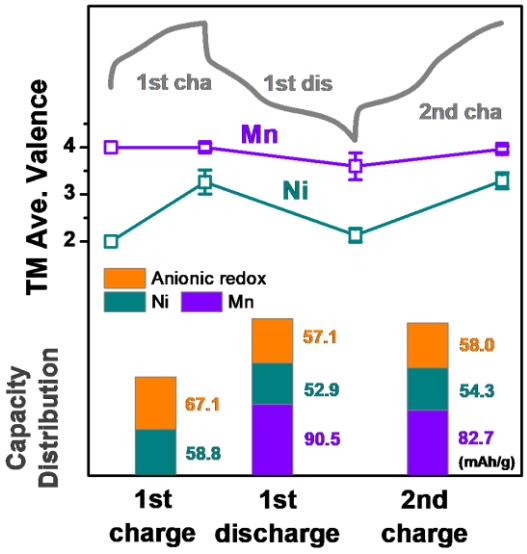

Figure 3. 13 The evolution of Ni/Mn average valence and capacity distributions of anionic/cationic redox behaviors in LLNMO at different charged states. The capacity contributions of anionic redox reactions are deduced by the total charge/discharge capacities and capacity distributions of Ni/Mn-based redox reactions.

3.6 Structural and electrochemical stability of LLNMO

At last, the structural and electrochemical stability in O2-type LLNMO was investigated by in-situ XRD measurement, XRD refinement and electrochemical tests. As displayed in **Figure 3.14a**, in-situ XRD measurement was employed to study the reversibility of structure evolution during Li^+ (de)intercalation processes. Upon the first charging, the (002), (004) and (006) peaks shifted to high angles, implying the decreasing of c-lattice parameter. Furthermore, these peaks shifted to original positions during the first discharge process, indicating the reversible structure evolution can be achieved upon the initial cycle. Moreover, no phase transition can be observed in

LLNMO during two cycles, delivering trigonal O2-type layered structure. After 50 cycles, the O2-type structure can be well preserved, which was characterized by ex-situ XRD. As depicted in **Figure 3.14b**, it demonstrates the LLNMO possesses the outstanding structural stability upon cycling. Moreover, as shown in **Figure 3.14c**, both normalized discharge curves and dQ/dV peaks proved the two plateaus can be maintained, implying the voltage decay induced by spinel phase was availably restrained.[48] Even at lower current density, as shown in **Figure 3.14d**, the slight capacity loss of 0.15 % per cycle and outstanding coulombic efficiency was obtained during 100 cycles. These results demonstrate that O2-type LLNMO harvested the admirable structural and electrochemical stability upon cycling.

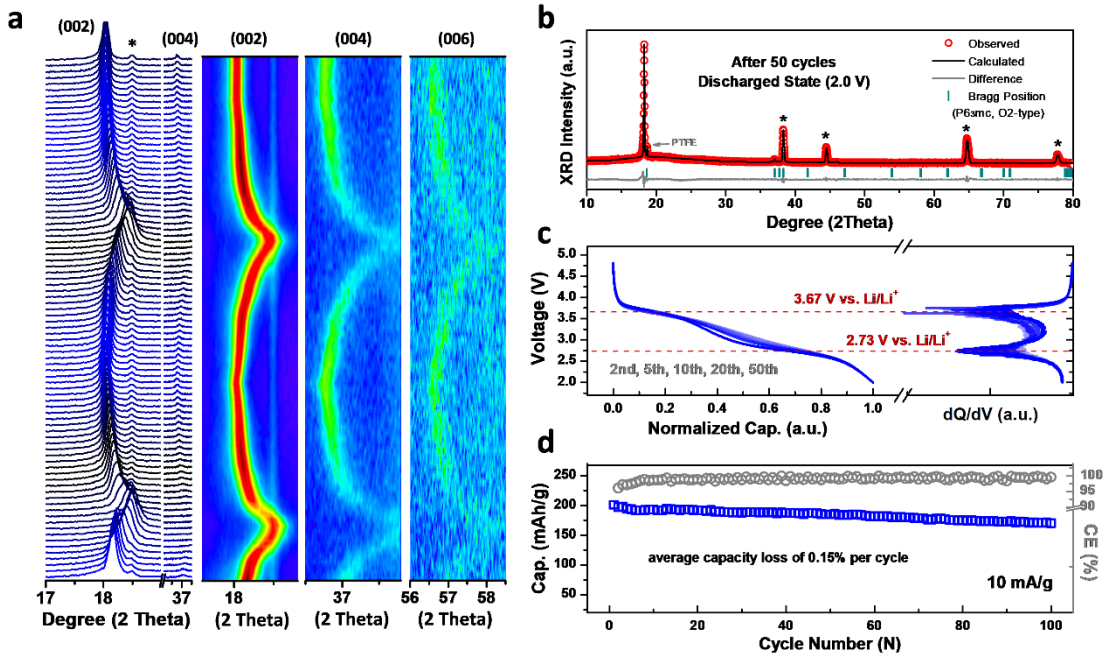

Figure 3. 14 a) In-situ XRD of LLNMO upon the first two cycles. b) The XRD patterns of LLNMO after 50 cycles. c) The normalized discharge curves and the corresponding dQ/dV profiles of LLNMO electrode. d) The discharge capacity and coulombic efficiency of LLNMO upon 100 cycles.

3.7 Summary and conclusions

O2-type LLNMO was developed by the chemical Li^+/Na^+ ion exchange method from P2-type NLNMO. Within the O2-type Li-excess cathode, the layered/spinel phase transition and irreversible oxygen release can be restrained, displaying the excellent

structural and electrochemical stability upon cycling. As a comparison, a similar O2-type oxide was also prepared by the electrochemical ion exchange from same Na-based precursor. It displayed the inferior electrochemical performance. From the aspect of methodology, chemical ion exchange is a forceful route to obtain the superior O2-type Li-excess cathode materials. Moreover, the cationic redox reactions in optimized O2-type layered LLNMO were clearly assigned and quantified, in which the integral method was performed. Furthermore, the capacity distributions of oxygen redox reactions have been clarified, which is important to understand the charge compensation mechanisms of Li-rich/excess oxide cathodes. Herein, not only methodology optimization was provided, but also the guide for structural design of high-energy-density Li-rich/excess cathodes was revealed.

Chapter 4. Stabilizing oxygen redox reactions in a O3-type layered oxide cathode constructed by Li-deficient pristine state

4.1 Introduction

With the speedy expansion of the electric vehicle industries in recent decades, the Li-ion battery systems should be further improved to effectively solve the problem of range anxiety.[9] To break through the bottleneck of energy density of existing Li-ion batteries, cathode material should be further improved because the commercial cathodes displayed relatively lower specific capacity than that of anode materials, which greatly decreases the energy density of full cell.[26]

Recently, by means of oxygen redox chemistry, the available capacity of Li-rich cathode materials reaches higher value than theory capacity triggered by TM-based redox reactions.[79-80] For typical Li-rich oxides, they have the chemical formula as $xLi_2MnO_3 \cdot (1-x)LiTMO_2$. The prototype Li-rich material, Li_2MnO_3 displays a charming charge capacity of more than 400 mAh g^{-1} upon first charging, which only originates form lattice oxygen oxidation reactions.[81] However, the Li_2MnO_3 electrode displays limited reversible capacities of less than 200 mAh g^{-1} during discharge process, which combines the Mn and oxygen reduction reactions simultaneously.[81] The serious irreversible capacity upon initial cycle was ascribed to excessive oxidation. The final product is the oxygen molecule, which is hard to be reversibly reduced during discharging.[81] What's worse, the oxygen loss accelerates harmful layered/spinel phase transition induced by irreversible TM migration, which causes further structural distortion and electrochemical decay during long-term cycling.[68] Thus, it is important to resolve and address these problems from the aspect of structural modification.[82] Besides, the complex charge compensation mechanisms of Mn-based and O-related redox reactions should be clearly clarified.

Herein, we designed a unique O3-type Li-excess layered cathode material

$Li_{0.6}[Li_{0.2}Mn_{0.8}]O_2$ (LMO).Compared with typical O3-type Li-rich oxides, the AM layer within LMO presents Li-deficient state while TM layer displays Li-excess state. By tuning Li proportion in AM layer, the lattice oxygen loss can be effectively restrained. Moreover, by achieving the Li substitution within TM layer, a high discharge capacity can be achieved. Besides, by using comprehensive spectroscopic characterizations, the mechanisms of Mn/O-related redox reactions were clearly clarified. Finally, the stable reversible structural evolution and Li migration were detected by in-situ XRD and ssNMR.

4.2 Structural and electrochemical characterizations of $Na_{0.6}[Li_{0.2}Mn_{0.8}]O_2$

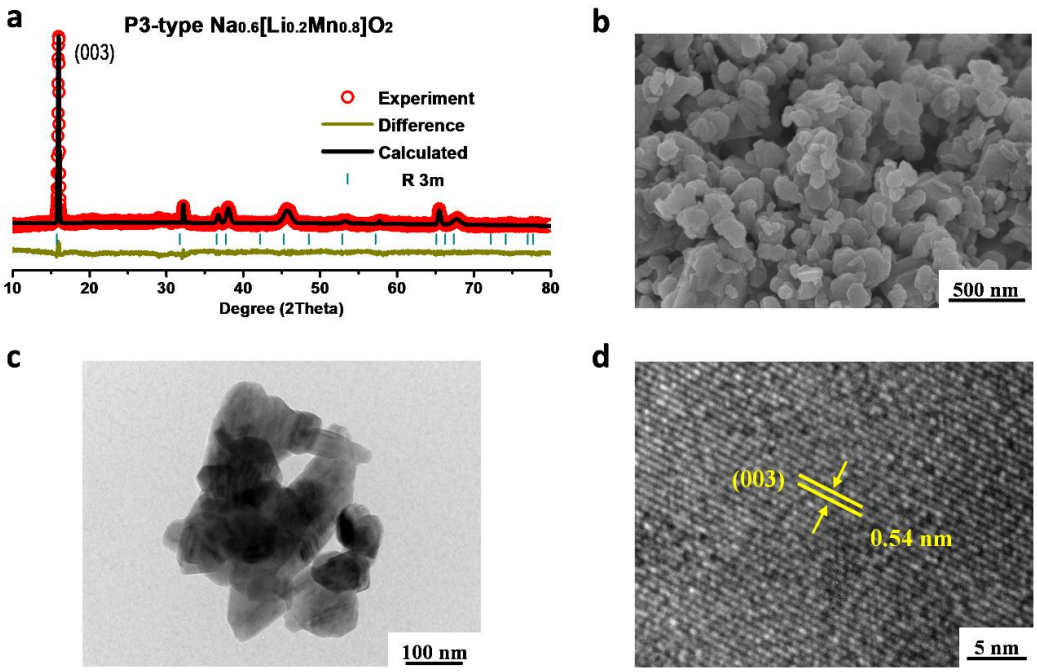

Figure 4. 1 a) XRD patterns of $Na_{0.6}[Li_{0.2}Mn_{0.8}]O_2$ and the corresponding results of Rietveld refinement. The b) FESEM, c) TEM and d) HRTEM results of the $Na_{0.6}[Li_{0.2}Mn_{0.8}]O_2$.

To obtain the Li-deficient O3-type $Li_{0.6}[Li_{0.2}Mn_{0.8}]O_2$, Na-based precursor P3-type $Na_{0.6}[Li_{0.2}Mn_{0.8}]O_2$ was designed and obtained via traditional solid-state reactions at high temperature. The experimental details were shown in experiment section 3.1.1. The Rietveld refinement of XRD and ICP were used to study the detailed parameters

and chemical composition. Meanwhile, the FESEM and TEM as well as HRTEM were employed to observe the morphology of $Na_{0.6}[Li_{0.2}Mn_{0.8}]O_2$.

Table 4. 2 Refined crystallographic parameter obtained by Rietveld analysis for $Na_{0.6}Li_{0.2}Mn_{0.8}O_2$. S.G. *R3m* a = b = 2.8764(8) Å, c = 16.8564(6) Å, α = β= 90°, γ = 120°, R_{wp} = 8.1 %, χ^2 = 2.94.

Atom	Site	x	y	z	Occ	Uiso
Na1	3a	0	0	0.1948(1)	0.60	0.03212
Li1	3b	0	0	0	0.19	0.01846
Mn1	3b	0	0	0	0.81	0.00698
O1	3c	0	0	0.3930(3)	1	0.01420
O2	3c	0	0	0.3930(3)	1	0.01724

Table 4. 2 Stoichiometry from ICP results of $Na_{0.6}Li_{0.2}Mn_{0.8}O_2$.

elements	content (mg/L)	mol ratio	Valence
Na	2.28	0.60	+1
Li	0.23	0.20	+1
Mn	7.26	0.81	+4

As depicted in **Figure 4.1a** and **Table 4.1**, the calculated pattern calculated by GSAS2 fitted well with the experimental data of $Na_{0.6}[Li_{0.2}Mn_{0.8}]O_2$, providing the accurate fitting results with limited error of R_{wp}=8.1 %, χ^2 = 1.46. It proves the Na-based $Na_{0.6}[Li_{0.2}Mn_{0.8}]O_2$ was precisely indexed as the trigonal P3-type structure with *R3m* space group. The refined parameters are a = b = 2.8764(8) Å, c = 16.8564(6) Å, α = β = 90° and γ = 120°. The P3-type layered oxide possesses the ABBCCA oxygen stacking arrangement. Owing to the absence of superlattice peaks in range of 20°-30°, the Li/Mn in TM layer occupies the octahedral sites irregularly and Na in AM layer occupies the trigonal prismatic sites. Besides, the chemical composition was confirmed by ICP shown in **Table 4.2**, delivering the chemical formula of $Na_{0.6}[Li_{0.19}Mn_{0.81}]O_2$, which meets our expectation and the value is within the limited error range. Therefore, the Na-based $Na_{0.6}[Li_{0.2}Mn_{0.8}]O_2$ can be demonstrated as a Na-deficient P3-type layered

oxide. As displayed in **Figure 4.1b** and **Figure 4.1c**, the FESEM and TEM images proved that the morphology of P3-type $Na_{0.6}[Li_{0.2}Mn_{0.8}]O_2$ was the nanosheets with a wide diameter distribution from 50 to 300 nm. As depicted in **Figure 4.1d**, the HRTEM measured an interlayer distance of 0.54 nm, which is agreement with the interplanar spacing of (003) peak.

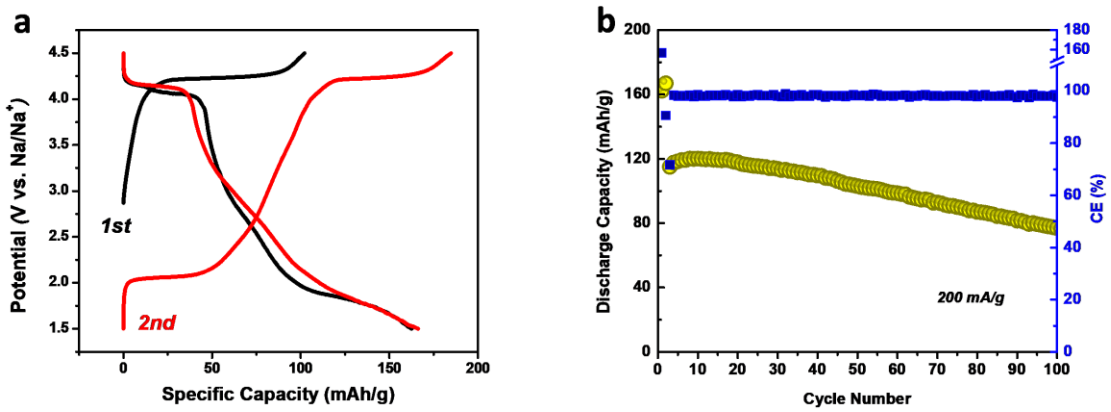

Figure 4. 2 The charge and discharge profiles of $Na_{0.6}Li_{0.2}Mn_{0.8}O_2$. And the discharge capacity and coulombic efficiency upon 100 cycles.

Moreover, the electrochemical characterizations were investigated by galvanostatic charge-discharge tests. As displayed in **Figure 4.2a**, the charge and discharge curves of $Na_{0.6}[Li_{0.2}Mn_{0.8}]O_2$ were obtained in Na half-cell between 1.5 and 4.5 V at 10 mA g^{-1}. The P3-type electrode displayed the reversible plateau with typical reversible oxygen redox behaviors. As depicted within **Figure 4.2b**, the cycling performance tested at 200 mA g^{-1} suggests the electrochemical stability of oxygen redox is poor, which induces the rapid capacity deterioration during cycling.

4.3 Structural and electrochemical characterizations of LMO

The Li-deficient O3-type LMO can be obtained from Na-based precursor P3-type $Na_{0.6}[Li_{0.2}Mn_{0.8}]O_2$ via chemical ion exchange strategy. The experimental details were shown in experiment section 3.1.2. The Li^+/Na^+ ion exchange can be realized in molten salts at high temperature. The schematic diagram of the chemical Li^+/Na^+ ion exchange process is shown in **Figure 4.3**. The XRD Rietveld refinement and ICP were employed to evaluate the lattice parameters and chemical composition. As shown in **Figure 4.4a**

and Table 4.3, the calculated pattern calculated by GSAS2 fits well with the experimental XRD pattern of $Li_{0.6}[Li_{0.2}Mn_{0.8}]O_2$, supplying the precise fitting results with low error of R_{wp}=7.4 %, χ^2 = 2.48. It proves that Li-based LMO was precisely indexed as the trigonal O3-type structure with $R\bar{3}m$ space group. The refined parameters are a = b = 2.8455(8) Å, c = 14.4254(6) Å, α = β = 90° and γ = 120°. The O3-type LMO displays the oxygen stacking arrangement of ABCABC in a unit.[30] Since the chemical Li^+/Na^+ ion exchange only occurred within AM layer, the compositions and arrangements of TM layer can be well maintained. Therefore, the Li/Mn arrangement within TM layer was irregular. After the chemical ion exchange process, the equivalent Na^+ ions were substituted by Li^+ ions.[83] The evolution of coordination environment within AM layer during the ion exchange was from trigonal prismatic NaO_6 to octahedral LiO_6.[63]

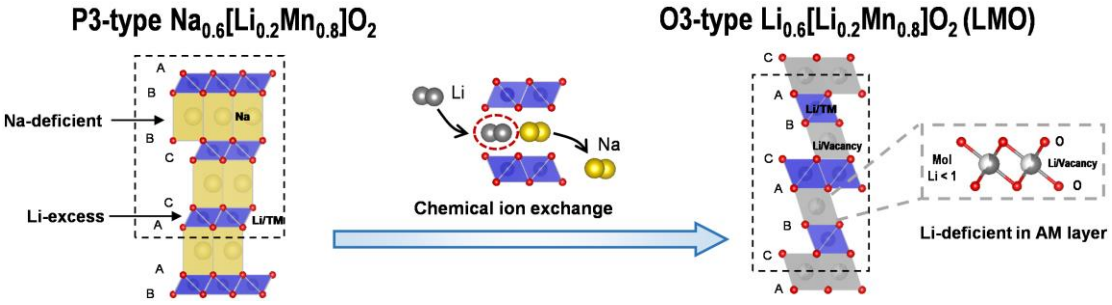

Figure 4. 3 The schematic diagram of the preparation of O3-type LMO obtained from P3-type $Na_{0.6}Li_{0.2}Mn_{0.8}O_2$ by chemical ion exchange strategy.

As shown in **Table 4.4**, the ICP results of LMO show that almost all sodium ions can be exchanged, which removes out of AM layer within layered structure. However, a trace amount of sodium ions (0.008 mol) can reside within AM layer, which has slight effect on the chemical formula of LMO. The remaining sodium ions should be ignored in obtained LMO. More importantly, the Li and Mn ions within TM layer can be well preserved. Therefore, these results prove that the chemical formula of LMO, which demonstrates the layered structure, the composition and arrangement of TM layer can be preserved during the ion exchange process, which is beneficial for design and preparation Li-rich/excess oxides form Na-based precursors.

Table 4. 3 Refined crystallographic parameters by Rietveld analysis for LMO. Space group of $R\bar{3}m$, a = b = 2.8455(8) Å, c = 14.4254(6) Å, α = β = 90°, γ = 120°, Rwp=7.4 %, χ2 = 2.48. The Li occupancies are constrained with the ICP results.

Atom	Site	x	y	z	Occ	Uiso
Li1	3a	0	0	0	0.60	0.02882
Li2	3b	0	0	0.5	0.20	0.07467
Mn	3b	0	0	0.5	0.80	0.03833
O1	6c	0	0	0.2408(3)	1	0.02784
O2	3c	0	0	0.3930(3)	1	0.03126

Table 4. 4 Stoichiometry from Inductively Coupled Plasma results of LMO.

elements	content (mg/L)	mol ratio	valence
Na	0.03	0.008	+1
Li	0.86	0.8	+1
Mn	6.81	0.8	+4

As displayed in **Figure 4.4b**, the first two charge-discharge curves of LMO were evaluated by galvanostatic test in Li half-cell. During the first charging, LMO electrode delivered an obvious plateau with charge capacity of 197 mAh g^{-1}, which corresponds to the approximate 0.6 mol Li ions removal. The charge capacity only can be contributed by oxygen oxidation reactions because the other active element cannot be oxidized to higher oxidation state in the layered structure. The solid evidence of XAS and in-situ Raman will be provided in section 4.3 and 4.5. Subsequently, more Li ions inserted in LMO during the initial discharge, delivering the estimated chemical formula of $Li_{1.13}Mn_{0.8}O_2$, which is calculated by the first discharge capacity. Within the low voltage region, a plateau occurred at approximate 3 V, which corresponds to the Mn reduction reaction during Li intercalation process. Upon the second charging process, the charge profile exhibited the S shape curve with two obvious plateaus located at about 3.0 V and 4.5 V, where the charge process includes cationic Mn-based and

oxygen-related oxidation reactions. Notably, the second discharge process displayed the high reversible capacity of 329 mAh g^{-1}, which can be calculated as approximate 1 mol Li^+ ions inserted into the layered structure. Based on the cathode material, LMO can achieve the excellent energy density of 1100 Wh kg^{-1}. Besides, the LMO electrode harvested the excellent cycling performance. As shown in **Figure 4.4c**, LMO still displayed the outstanding capacity retention at 300 mA g^{-1}, in which the limited capacity loss of 0.045 % can be obtained during the 500 cycles. These results suggest that the LMO electrode would harvest the reversible anionic/cationic redox reaction processes upon cycling.

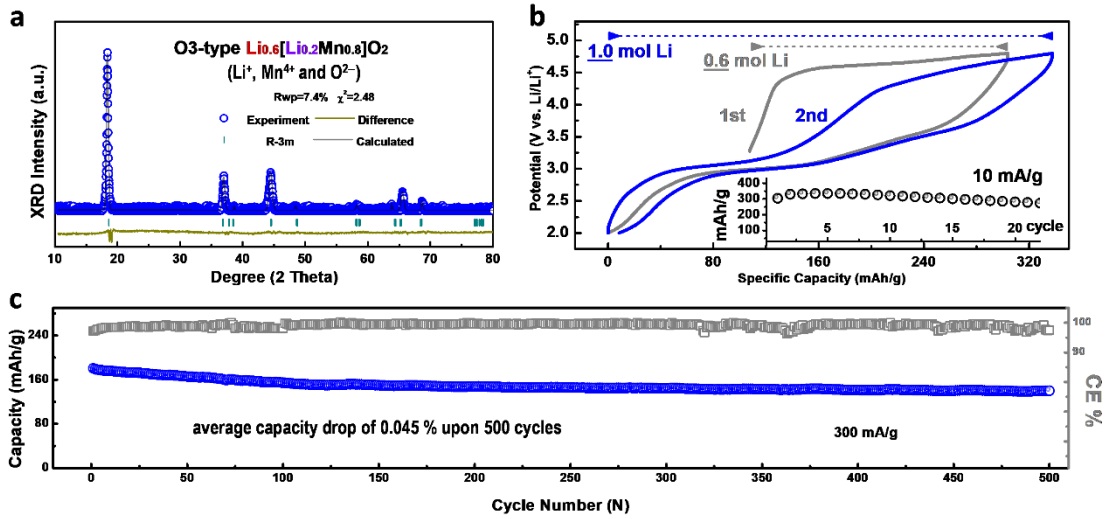

Figure 4. 4 a) XRD pattern of LMO and the corresponding results of Rietveld refinement. b) The charge and discharge curves of LMO. The insert showed the discharge capacity of LMO upon 20 cycles at 10 mA g^{-1}. c) The discharge capacity and coulombic efficiency of LMO upon 500 cycles at 300 mA g^{-1}.

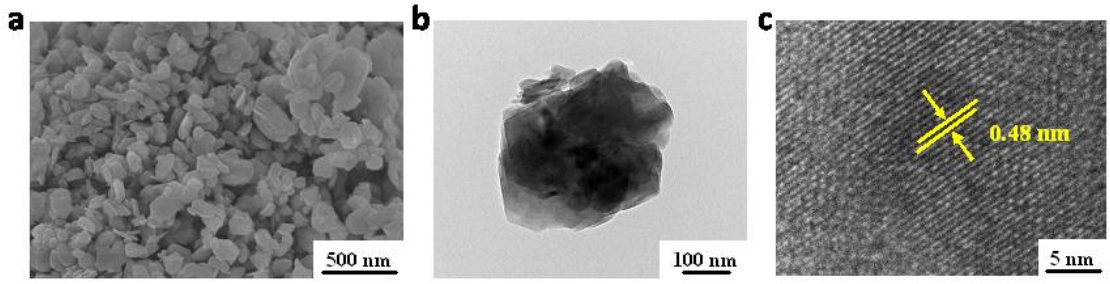

Figure 4. 5 The a) FESEM, b) TEM and c) HRTEM results of the pristine LMO.

Moreover, based on FESEM and TEM results displayed within **Figure 4.5a** and **Figure 4.5b**, it is not hard to find that the LMO inherited the morphology of

$Na_{0.6}[Li_{0.2}Mn_{0.8}]O_2$. It exhibited the morphology of independent nanosheets with the diameter distributions from 50 to 300 nm. From the HRTEM results shown in **Figure 4.5c**, the interlayer spacing of 0.48nm can be measured, which fitted well with the interlayer distance of (003) plane.

4.4 The oxygen behaviors in LMO

4.4.1 The combination of in-situ Raman and DEMS

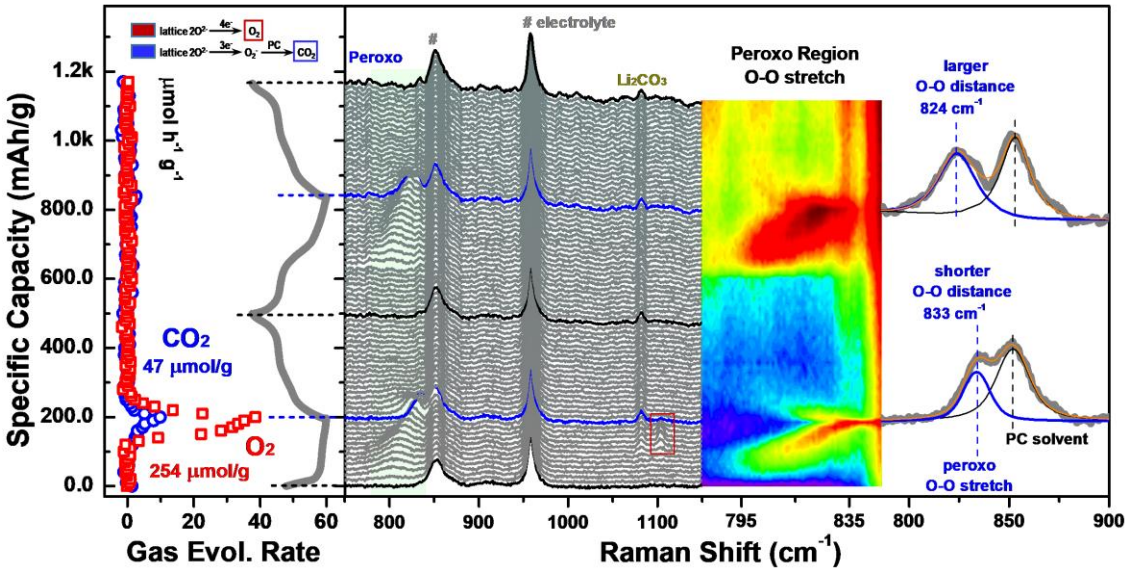

Figure 4. 6 The combination of in-situ DEMS and Raman measurements of LMO upon two cycles.

The reversible/irreversible oxygen redox reactions in LMO electrode were identified by the combination of in-situ DEMS and Raman, as shown in **Figure 4.6**. The in-situ DEMS measurement is generally regarded as a quantitative method to collect the information of gas (such as O_2 and CO_2) evolution during Li^+ (de)intercalation processes.[84] The Raman is also recognized as an efficient measurement to detect oxygen species such as peroxo and superoxo species. The combination of in-situ DEMS and Raman is beneficial for comprehensively clarifying the irreversible and reversible oxygen redox reactions. Upon the first charging process, a newly produced peak appeared in the range from 780 to 850 cm^{-1} (peroxo O–O stretch region), in which the intensity of the peak increased, and the location has a blue shift process.[85-86] Subsequently, the peak gradually disappeared during the initial discharging process.

Furthermore, upon the second cycle, the reversible variation trend of the peroxo signal occurred again in peroxo O–O stretch region. During the initial two cycles, the reversible trends of peroxo signal demonstrated the lattice oxygen can be oxidized to oxidized lattice oxygen at charged states, and then it can be well reduced to lattice oxygen after discharging. In corresponding color mapping, it is not hard to find that the peak in second cycle exhibited higher intensity than that of first cycle within the peroxo O–O stretch region. It indicates more reversible capacity can be triggered by oxygen oxidation during second charge. The electrochemical data also proved the deduction during the initial two cycles. Moreover, the larger O–O distance (corresponding to 824 cm^{-1}) was detected at second charged state also demonstrate more reversible and moderate oxygen oxidation reaction can be obtained, whereas the shorter O–O distance (corresponding to 833 cm^{-1}) was detected upon first charge. The drastic decreasing of O–O distance is easy to induce the formation of superoxo species, which is easy to be transformed to gaseous O_2. Notably, a sharp peak located at around 1104 cm^{-1} can be detected upon the initial charge.[87] The signal can be ascribed to the appearance of superoxo during the first charging. However, the signal of superoxo species disappeared after the first charge. During the subsequent cycles, the unfavorable products cannot be detected, indicating the oxygen redox reactions in LMO are stable after first oxygen activation process.[88] In DEMS results, superoxo species can be further oxidized to O_2 with the decreasing of O–O distance. The 254 μmol/g gaseous O_2 can be quantified upon the initial charging. Besides, the in-situ DEMS measurement also identified the evolution of CO_2 with 47 μmol/g. The formation of CO_2 has two possible sources.[89] The first is the decomposition of Li_2CO_3 caused by the superoxo-induced nucleophilic reaction. The other source is that electrolyte decomposition caused by electrochemical driving force in high voltage region. During the subsequent cycles, the lattice oxygen loss cannot be observed, demonstrating the reversible oxygen redox reactions can be harvested. In general, the combination of in-situ Raman and DEMS proves the reversible oxygen redox behaviors have been realized in the LMO electrode.

4.4.2 The mechanisms of irreversible and reversible oxygen behaviors

Through in-situ Raman and DEMS analysis, the mechanisms of oxygen redox reactions can be proposed, which is shown in **Figure 4.7**. Upon the charging process, when the energy of hybrid between σ* and Mn 3d orbital was above the Fermi level, it generated the fully occupied π*, π and σ orbitals. The situation allows the reversible oxygen redox reaction can be obtained, in which the lattice oxygen only can be oxidized to peroxo species. Furthermore, with the decreasing of energy of Fermi level, π* orbital provided electron upon deep charging process, delivering the formation of superoxo species. The process would produce the partial empty π* orbital. When the gaseous O_2 can be generated, the π* orbital was half occupied.[90] These over-oxidized products such as superoxides and gaseous O_2 would reduce the covalency to Mn^{4+}, resulting in the serious structural rearrangement such as layered/spinel phase transition, which further causes the serious voltage decay and capacity deterioration.

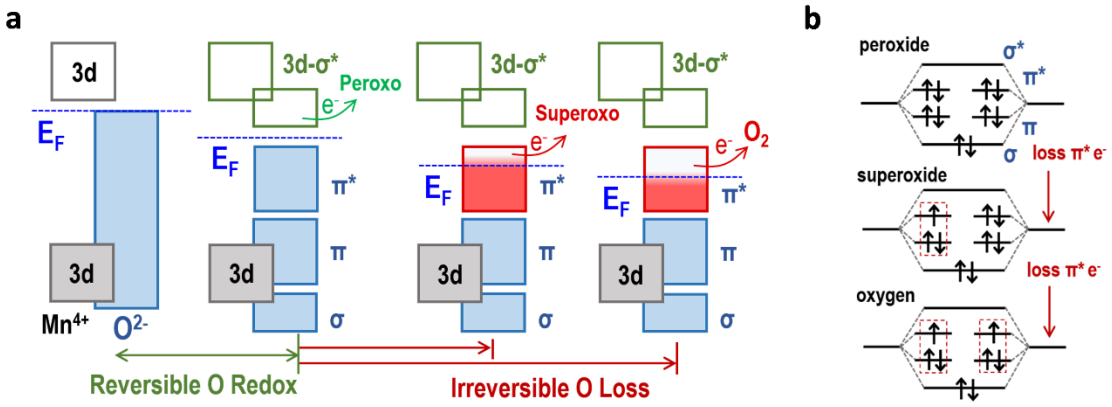

Figure 4. 7 The schematic diagram of the evolutions of a) band and b) electron structures upon the oxygen activation processes.

4.5 Structural evolutions of LMO

4.5.1 The ex-situ Raman of LMO

To identify the structural stability of LMO during cycling, the ex-situ Raman spectra and corresponding the electrochemical normalized discharge curves were shown in

Figure 4.8. Herein, the typical Li-rich material, $Li[Li_{0.33}Mn_{0.67}]O_2$ (Li_2MnO_3), was selected as a reference sample to compared the structural evolution during cycling. As displayed in **Figure 4.8a**, after 20 cycles, the LMO electrode exhibited the excellent discharge voltage retention, delivering the limited voltage decay (0.18 and 0.16 V). On the contrary, Li_2MnO_3 showed the serious voltage decay (0.34 and 0.66 V) and the obvious shape changes in normalized discharge profiles. As shown in **Figure 4.8b**, the ex-situ Raman spectra clarified the reason for the serious voltage decay in Li_2MnO_3. It was generally attributed to the formation of spinel structure (cubic) during the initial 20 cycles. As a sharp comparison, the LMO harvested the excellent structural stability, delivering the absence of layered/spinel phase transition.

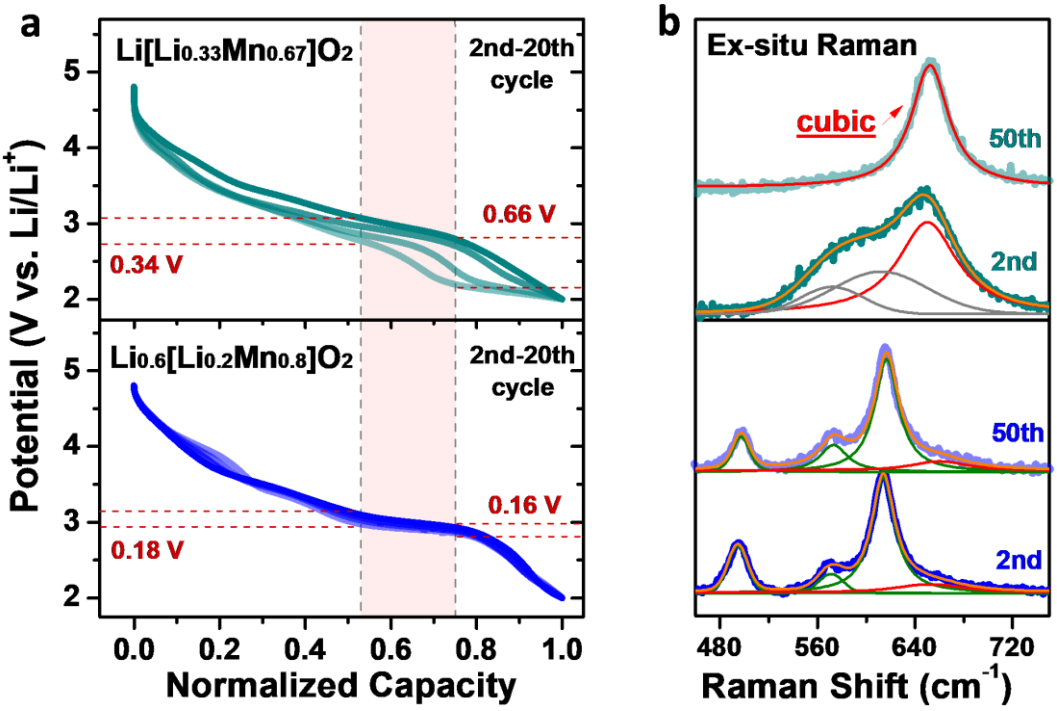

Figure 4. 8 a) The 2nd-20th discharge profiles of LMO and $Li[Li_{0.33}Mn_{0.67}]O_2$ (Li_2MnO_3) and b) the ex-situ Raman spectra of the two electrodes after 2nd and 50th cycles.

4.5.2 The in-situ XRD of LMO

In-situ XRD measurement was also investigated to observe the phase transition and structural evolution of LMO, which is shown in **Figure 4.9**. Upon the first Li^+ deintercalation process, the position of (003) peak shifted to high diffraction angle.

Meanwhile, the location of peak only had a slight change. These evolutions are similar to that in Li_2MnO_3 with pure oxygen oxidation reactions during the first charging process. Furthermore, the location movement of both (003) and (101) peak upon the second charging was a reverse process of that during the first discharging. And then, the structural evolution upon the second discharge process displayed the similar shift compared to that during the initial discharging. Notably, no phase transition can be detected within the LMO electrode, demonstrating O3-type layered LMO had excellent structural reversibility and stability upon cycling. Besides, the peaks marked by * was contributed to Al form two parts. The first one is Al window in the cathode case. The other is from the Al current collector of cathode. These peaks have overlap with the characteristic peak of LMO, which affects the observation of the (104) peak.

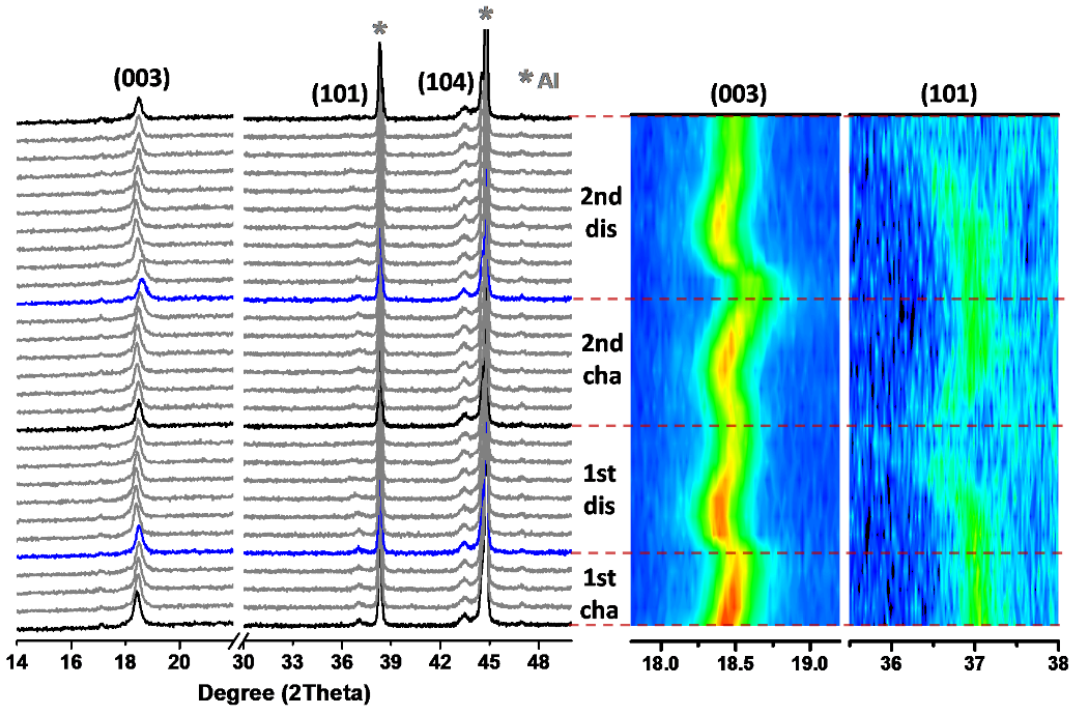

Figure 4. 9 In-situ XRD results of LMO upon the first two Li^+ (de)intercalation processes.

4.5.3 The ^{7}Li ssNMR measurement

To further investigate the Li migration pathways during charging and discharging, ^{7}Li ssNMR was performed, as shown in **Figure 4.10**. Owing to the Li^+ ions within LMO have two types of local environments, it is significant to clarify their influences

on oxygen redox behaviors and structural stability during cycling.[91-92] The resonance located at 1300~1650 ppm can be attributed to Li site in TM layer, and the resonance located at 500~1000 ppm can be assigned to Li locations in AM layers.[93-94] When charged to 4.8 V, approximate 0.2 mol Li ions resided within AM layer, whereas about 0.6 mol Li ions removed out of layered structure. It delivered the chemical formula of $Li_{0.2}Mn_{0.8}O_2$ with vacancy–oxygen–vacancy configuration along c-axis direction. When discharged to 2 V, the amount of Li^+ ions within AM layer increased to 85 %, delivering two local environments of 16 % Li–O–Li and 69 % Li–O–Mn configurations. Meanwhile, the content of Li^+ ions within TM layer also increased to 15 %, suggesting the Li migration between TM and AM layer was a reversible process, providing a stable foundation for the reversible anionic redox reactions and structure stability within LMO.

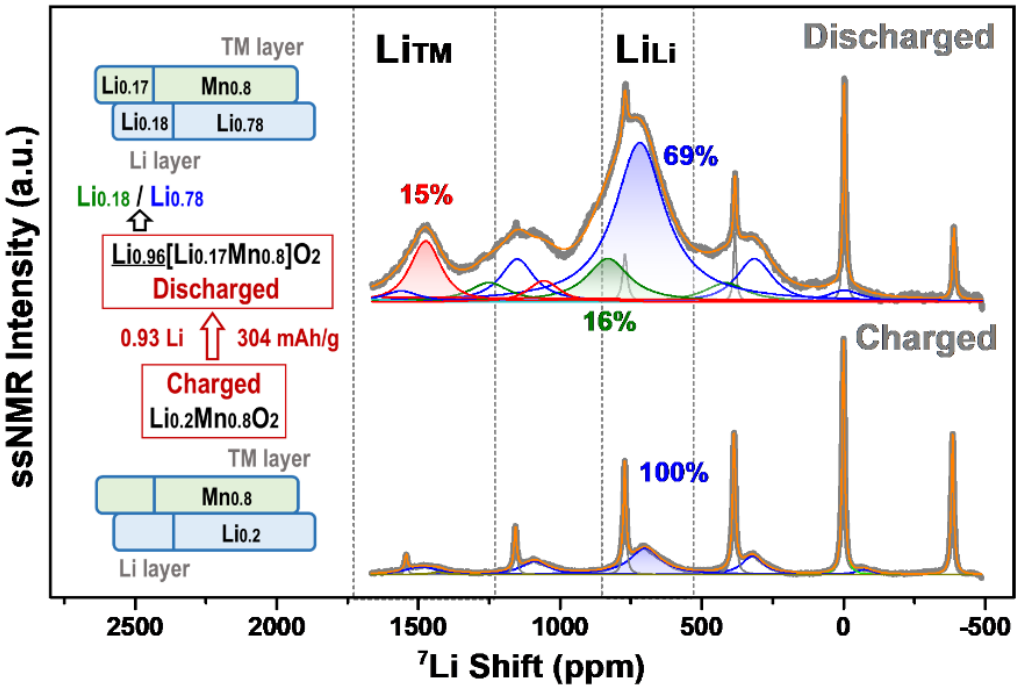

Figure 4. 10 ^{7}Li ssNMR spectra of LMO at first charged and discharged states.

4.6 Analysis of cationic/anionic redox reactions

4.6.1 The O K-edge and Mn L-edge soft XAS

To investigate the underlying charge compensation mechanisms based on cationic/anionic redox reactions, O K-edge and Mn L-edge soft XAS were employed.

As shown in **Figure 4.11**, the TEY mode with probe depth of ≈10 nm was employed to collect the surface information, and the TFY mode with probe depth of ≈100 nm was used to obtain the bulk information.[95] For O K-edge XAS spectra, it was generally classified as two sections. The energy of pre-edge region is below 535 eV and the energy of broad band region is above the value. Within pre-edge region, the peak located at 529.2 corresponds to the t_{2g} orbital, and the other peak centered at 531.8 eV corresponds to the e_g orbital.

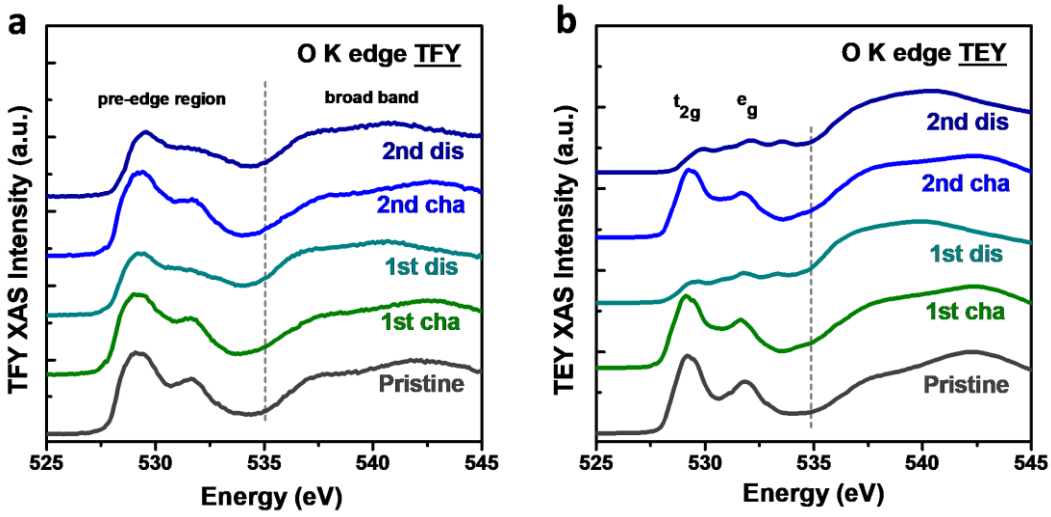

Figure 4. 11 The O K-edge XAS spectra of LMO obtained at a) TFY and b) TEY modes.

At charged states, both t_{2g} and e_g peaks showed higher intensity relative to the discharge states upon initial two cycles, where the intensity change mirrored both the number of unoccupied hybridized states and the contribution of oxygen to their wavefunction.[96] Upon the initial two Li^+ deintercalation processes, the increasing intensity revealed that the transition of electrons from O 1s to unoccupied t_{2g} and e_g orbitals of O 2p-Mn 3d hybridization.[97] Moreover, the TFY O K-edge XAS in pre-edge region also exhibited same variation tendency as TEY mode upon initial two cycles. However, the difference of peak intensity between 1st charged and 2nd charged states indicated that more oxygen-related capacities can be triggered in bulk materials during second charging process. Besides, the peak located at 533.3 eV can be detected in TEY spectra at discharge states, which is attributed to the existence of Li_2CO_3 in the

surface.[98] Furthermore, both in the broad band region (above 535 eV) of TEY and TFY O K-edge XAS, the peak shifts was originated from the cationic Mn^{4+}/Mn^{3+} redox reactions, which will be confirmed in subsequent Mn L-edge XAS part.

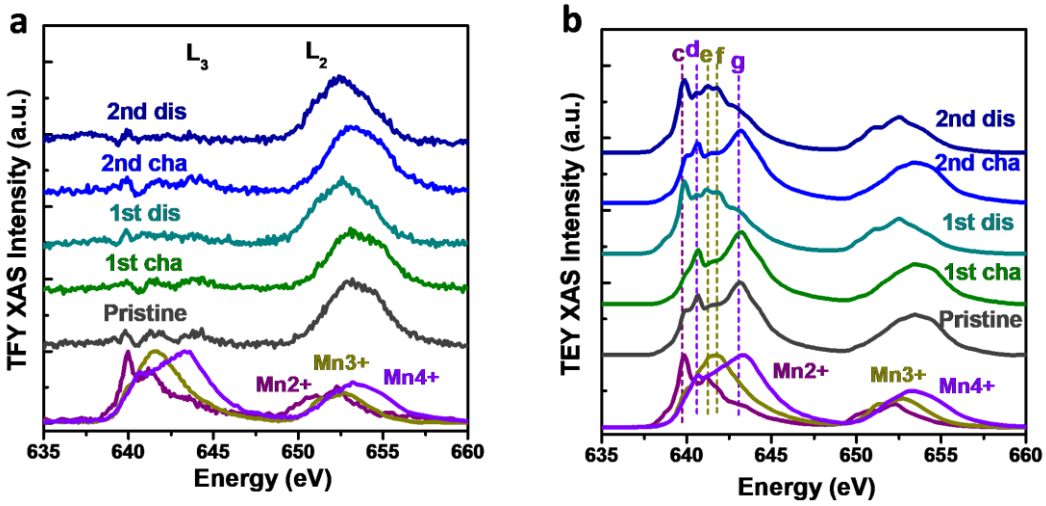

Figure 4. 12 Mn $L_{2,3}$-edge XAS spectra of LMO obtained at a) TFY and b) TEY mode at different states.

As shown in **Figure 4.12**, the variation of Mn oxidation states was also investigated based on the TFY and TEY mode. At pristine state, the oxidation state of Mn within LMO was dominant Mn^{4+} and negligible Mn^{3+}. Upon the first charging, both the intensity and position of L_3 and L_2 peaks kept unchanged, demonstrating the participation of hybridized O 2p-Mn 3d bonds that dominantly involved the changes in O-ligands in compensating charges given the dominant character of the oxidation state of Mn^{4+} both in surface and bulk material.[99] Therefore, Mn redox reactions were not significantly involved in the charge compensation during first charging. Thus, only oxygen oxidation reaction was contributed to the initial charge capacity. After discharging to 2 V, the L_3 and L_2 peaks both in TEY and TFY mode all shifted towards lower energy region, suggesting the reduction reaction (from Mn^{4+} to Mn^{3+}) occurred during discharge process. More intriguingly, when recharged to 4.8 V, the L_3 and L_2 peaks exhibited no obvious edge shift compared with that at the first charge state, which indicates reversible oxidation process of that all Mn^{3+} in LMO was oxidized to Mn^{4+} during second charging. After the second discharge process, the spectrum of discharged

LMO returned to the first discharge state, suggesting the reversible cationic redox processes have been achieved at the ending of discharge. Thus, a reversible evolution of the Mn electronic structure coupled with Li^+ (de)intercalation processes can be realized in LMO electrode.

4.6.2 The electrochemical reaction pathways of Li-rich/excess oxides

The two-component notation was generally used to show electrochemical reaction pathways of Li-rich $xLi_2MnO_3 \cdot (1-x)LiMO_2$ oxides during Li^+ (de)intercalation processes.[100] Here, our group developed a quarternary compositional phase diagram of Li_2MnO_3–$LiMO_2$–MnO_2–MnO_3 configuration, in which we added the MnO_3 region for the ternary compositional phase diagram of Li_2MnO_3–$LiMO_2$–MO_2. The MnO_3 consists of a Mn^{4+}, a O^{2-} and two O^-. By means of the Li_2MnO_3–$LiMO_2$–MnO_2–MnO_3 configuration, the reaction pathways of irreversible and reversible oxygen redox reactions can be clearly presented in the ternary compositional phase diagram. Upon the first charging, the LMO electrode entered the Li_2MnO_3–MnO_2–MnO_3 region, delivering the pure oxygen oxidation reactions, which follows the blue line. However, the LMO electrode suffered from the slight oxygen release (0.05 mol within chemical formula) during this process, which can be marked along the Li_2MnO_3–MnO_2 direction. Upon the initial discharging, the LMO electrode obtained the reversible oxygen redox reactions along the Li_2MnO_3–MnO_3 direction. For the typical Li-rich oxides, the black and red line exhibited the serious irreversible oxygen loss during the initial charge, and cationic transition metal were reduced to lower oxidation states compared with pristine state. [68, 95, 101] Therefore, we design the pathways toward the design of ideal Li-rich materials (green line) with more capacities triggered by oxygen redox reactions and less irreversible oxygen loss.

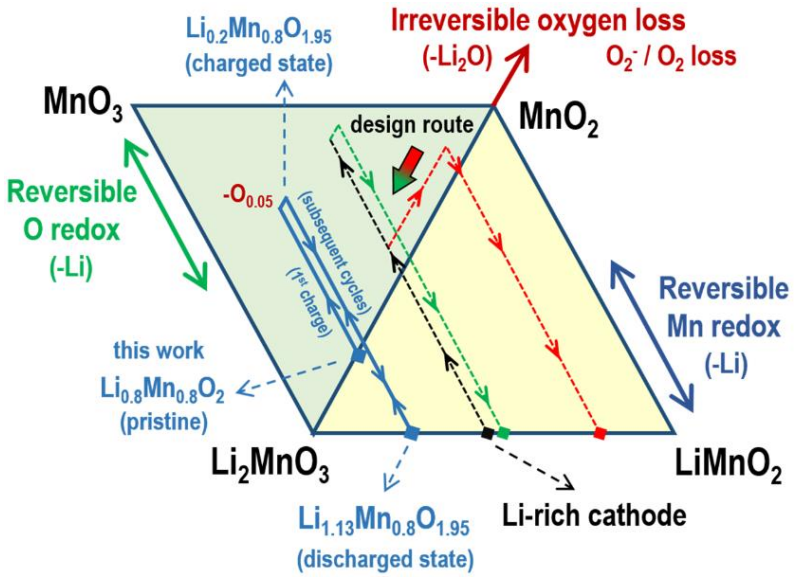

Figure 4. 13 The electrochemical reaction pathways of LMO (blue line) and typical Li-rich Mn-based oxides (black and red lines) in the compositional phase diagram. The design route (black and green lines) of idea Li-rich oxides was also provided.

4.7 Conclusions

In this work, we reported Li-deficient O3-type LMO as cathode material for Li battery system, harvesting high capacity and energy density contributed from reversible cationic/anionic redox reactions. Combined with DEMS and XAS analyses, all the capacity contributions of oxygen-related and Mn-based redox reactions were thoroughly quantified. Furthermore, the oxygen behaviors had been clarified and the corresponding reductive distortion mechanisms were proposed. Besides, the structure stability and reversible Li migration also provided a solid foundation of oxygen chemistry in long term cycling. Altogether, these findings provided feasible means to assess the reversibility of oxygen redox chemistry and new pathway for designing better Li-rich materials.

Chapter 5. General conclusions and perspectives

5.1 General conclusions

In the dissertation, developing the layered Li-excess materials is a promising route to greatly improve the energy density of Li-ion battery systems. Nevertheless, the utilization of layered Li-excess oxide materials has two main challenges. The first is serious lattice oxygen loss during the oxygen activation process. And the other is irreversible TM migration. These problems would induce severe capacity loss and voltage fade during cycling. To address the two challenges, on the one hand, we developed a novel O2-type Li-excess oxide, $Li_{0.66}[Li_{0.12}Ni_{0.15}Mn_{0.73}]O_2$, with novel oxygen stacking arrangement, which is distinct with the typical O3-type Li-rich/excess oxides. On the other hand, we designed a unique O3-type Li-excess layered cathode material, $Li_{0.6}[Li_{0.2}Mn_{0.8}]O_2$, with Li-deficient state within AM layer and Li-excess state in TM layer. The two challenges for layered Li-excess oxides can be well resolved in two novel cathodes, which can be attributed to the structural design and modification.

In **Chapter 3**, the O2-type $Li_{0.66}[Li_{0.12}Ni_{0.15}Mn_{0.73}]O_2$ was achieved as a novel cathode, which was obtained by chemical ion exchange strategy from Na-based precursor. It exhibits the layered structure and ABAC oxygen stacking arrangement. (**Chapter 3.2**) In the special structure, the harmful phase transition and oxygen release can be restrained, greatly boosting the structural and electrochemical stability. (**Chapter 3.3**, **3.4** and **3.6**) By contrast, a O2-type oxide obtained by electrochemical ion exchange strategy from same Na-based precursor displays serious oxygen release and voltage deterioration. (**Chapter 3.3** and **3.4**) Besides, the capacity contributions of Ni/Mn-based and oxygen redox reactions have been clearly quantified, further clarifying the complex charge compensation mechanism. (**Chapter 3.5**)

In **Chapter 4**, the modified O3-type $Li_{0.6}[Li_{0.2}Mn_{0.8}]O_2$ as cathode material was achieved by tuning the Li contents in TM and AM layer. Compared with the typical O3-type Li-rich oxides, the AM layer of the modified O3-type structure displays a special Li-deficient state, whereas the TM layer still maintains the Li-excess state. (**Chapter**

4.3) Benefitting from the Li−O−Li configuration, LMO also possesses the high charge capacity of 197 mAh g^{-1} contributed by pure oxygen oxidation during the first charging. Notably, the modified O3-type electrode possesses reversible capacity of 189 mAh g^{-1} upon discharging, which was triggered by the oxygen reduction reactions. Furthermore, adding the Mn-based redox activities, the high discharge capacity of 329 mAh g^{-1} was realized. (**Chapter 4.3**) Moreover, anionic/cationic redox behaviors were well assigned by XAS, DEMS and Raman measurements. Furthermore, the reversible Li migration proved by in-situ XRD and ssNMR also is beneficial for achieving the stable structure evolution upon long-term cycling. (**Chapter 4.4** and **4.5**)

In general, we provided a useful guide for rational design of excellent Li-rich/excess materials from the methodology aspect, in which the challenges of lattice oxygen release and irreversible TM migration can be well resolved. Moreover, deep insights of anionic and cationic redox behaviors are pointed out from the structural and electrochemical aspects. Nevertheless, much effort should further be devoted to realizing its practical application in the future.

5.2 Perspectives

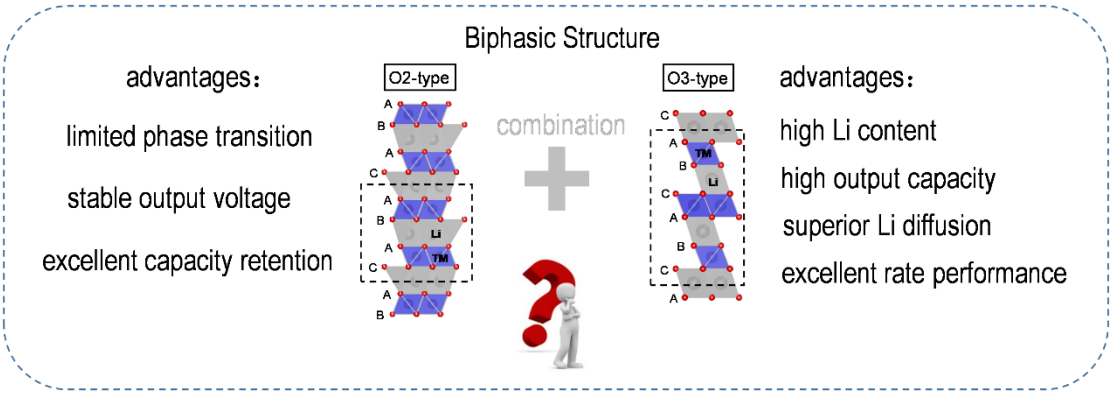

Figure 5. 1 The perspective of the combination of O2-type and O3-type structure in a biphasic structure.

According to the results obtained from this dissertation, O2-type structure processes the advantages such as excellent structural stability, stable output voltage and outstanding capacity retention. And O3-type structure harvests the prominent features such as high Li content, high output capacity and excellent performance. Herein, we

proposed a concept of biphasic structure in a material, as shown in **Figure 5.1**. The layered Li-rich/excess material with biphasic structure is expected to inherit the advantages of both O2-type and O3-type structures. If the design can be achieved, the biphasic Li-rich/excess oxide materials would display the high output capacity and excellent cycling performance at the same time. Thus, the combination of O2-type and O3-type structure might be a good choice for both structural and electrochemical stability in the systems of Li-rich/excess cathode to build better batteries in the future.

List of Publications

First author:

1. **Xin Cao**, Haifeng Li, Yu Qiao, Min Jia, Xiang Li, Jordi Cabana and Haoshen Zhou. Stabilizing anionic redox chemistry in a Mn-based layered oxide cathode constructed by Li-deficient pristine state. *Advanced Materials*. 2021, 33, 2004280.
2. **Xin Cao**, Haifeng Li, Yu Qiao, Min Jia, Ping He, Jordi Cabana and Haoshen Zhou. Achieving stable anionic redox chemistry in Li-excess O2-type layered oxide cathode via chemical ion-exchange strategy. *Energy Storage Materials*. 2021, 38, 1-8.

(The first two papers are related to this Ph.D. thesis.)

3. **Xin Cao**, Yu Qiao, Min Jia, Ping He and Haoshen Zhou. Ion-exchange: a promising strategy to design Li-rich and Li-excess layered cathode materials for Li-ion batteries. *Advanced Energy Materials*. 2021, DOI: 10.1002/aenm.202003972.
4. **Xin Cao** and Haoshen Zhou. An indicator of designing layered sodium-ion oxide materials. *Science Bulletin*. 2021, 66, 753-754.
5. **Xin Cao**, Haifeng Li, Yu Qiao, Xiang Li, Min Jia, Jordi Cabana and Haoshen Zhou. Stabilizing reversible oxygen redox chemistry in layered oxides for sodium-ion batteries. *Advanced Energy Materials*. 2020, 10, 1903785.
6. **Xin Cao**, Xiang Li, Yu Qiao, Min Jia, Feilong Qiu, Ping He and Haoshen Zhou. Restraining oxygen loss and suppressing structural distortion in a newly Ti-substituted layered oxide P2-$Na_{0.66}Li_{0.22}Ti_{0.15}Mn_{0.63}O_2$. *ACS Energy Letters*. 2019, 4, 2409-2417.
7. **Xin Cao**, Haifeng Li, Yu Qiao, Min Jia, Hirokazu Kitaura, Jianan Zhang, Ping He, Jordi Cabana and Haoshen Zhou. Structure design enables stable anionic and cationic redox chemistry in a T2-type Li-excess layered oxide cathode. **Submitted to Energy & Environmental Science.**

Acknowledgements

In the twinkling of an eye, I have been studying at the University of Tsukuba for three years. During my PhD period, too many people offered me warm help and encouragement for my studies and daily life. I am enormously grateful to them.

In the first place, I want to express my heartfelt thanks to my supervisor Prof. Haoshen Zhou. He offered me many careful guidance for research works, which has benefited me a lot. He always tells us a researcher should challenge the authority with question and break conventions in previous research works. Moreover, he always teaches us the way and logic of addressing problems, which is useful for my research and life. Besides, his rigorous academic attitude encouraged me to take everything earnestly. Indeed, I have learnt a lot from him.

In the next place, I would like to express my gratitude to my vice-supervisors, Prof. Masayoshi Ishida and Associate Prof. Hirohisa Aki. They are very responsible for my development in school. They regularly care about my research progress and living environment in University of Tsukuba. Especially, thanks to Prof. Masayoshi Ishida, Associate Prof. Hirohisa Aki, Dr. Eunjoo Yoo and Dr. Hirokazu Kitaura. They provided to the useful suggestions from my graduation presentation, which significantly improves the quality of presentation and dissertation.

Thirdly, I am grateful to the Dr. Yu Qiao and Dr. Xiang Li for their kind help. They taught me the experiment details and the analysis of experimental data, which promotes my research process. They always put forward many useful suggestions and did not hesitate to share their ideas for my research work. Besides, we usually go sightseeing together and have been to many Japanese attractions. Words cannot express how thankful I am.

Fourth, I want to express the depth of my gratitude to my group numbers. Dr. Hirofumi Matsuda, Dr. Eunjoo Yoo and Dr. Hirokazu Kitaura always care about our safety in National Institute of Advanced Industrial Science and Technology. Mr. Jun Okagaki helped me to solve the problem many times whenever I was in trouble. I also benefit from Dr. Yarong Wang, Dr. Qi Li, Dr. Feilong Qiu, Dr. Linlin Wang, Dr. Han

Deng, Dr. Min Jia, Mr. Xingyu Zhu and Prof. Jianan Zhang. They provided many warm helps both on my research works and daily life. Besides, I want to thank Dr. Zhi Chang, Mr. Huijun yang and Mr. Jianming Sun. We are still working side by side during the COVID-19 period.

Furthermore, I want to appreciate Dr. Yanbing Wu, Dr. Chenzhu Yin and other friends I met because of badminton. We always play badminton together, including Dr. Xiang Li and Mr. Huijun Yang. We shared many happy times.

Besides, I am truly grateful for the financial support from China Scholarship Council, which allows me to concentrate on scientific research without worrying about the cost of living.

At last, I would like to extend my deep gratefulness to my family members. My father Junxiang Cao, my mother Aiping Hou, and my grandfather and grandmother give me many spiritual supports. Finally, sincerely thanks to my wife Yinyin Jia, your love and care are the greatest fortune of my life. I hope we will have a happy time for the rest of our life.

REFERENCE

[1] Omer, A. M., Energy, environment and sustainable development. *Renew. Sustain. Energy Rev.* **2008,** *12* (9), 2265-2300.
[2] Bose, B. K., Global Warming: Energy, Environmental Pollution, and the Impact of Power Electronics. *IEEE Ind. Electron. Mag.* **2010,** *4* (1), 6-17.
[3] Armaroli, N.; Balzani, V., Towards an electricity-powered world. *Energy Environ. Sci.* **2011,** *4* (9), 3193-3222.
[4] Crabtree, G., The coming electric vehicle transformation. *Science* **2019,** *366* (6464), 422-424.
[5] Hadjipaschalis, I.; Poullikkas, A.; Efthimiou, V., Overview of current and future energy storage technologies for electric power applications. *Renew. Sustain. Energy Rev.* **2009,** *13* (6), 1513-1522.
[6] Armand, M.; Tarascon, J.-M., Building better batteries. *Nature* **2008,** *451* (7179), 652-657.
[7] Winter, M.; Brodd, R. J., What Are Batteries, Fuel Cells, and Supercapacitors? *Chem. Rev.* **2004,** *104* (10), 4245-4270.
[8] Pollet, B. G.; Staffell, I.; Shang, J. L., Current status of hybrid, battery and fuel cell electric vehicles: From electrochemistry to market prospects. *Electrochim. Acta* **2012,** *84*, 235-249.
[9] Li, W.; Erickson, E. M.; Manthiram, A., High-nickel layered oxide cathodes for lithium-based automotive batteries. *Nat. Energy* **2020,** *5* (1), 26-34.
[10] Raccichini, R.; Amores, M.; Hinds, G., Critical Review of the Use of Reference Electrodes in Li-Ion Batteries: A Diagnostic Perspective. *Batteries* **2019,** *5* (1), 12.
[11] Su, X.; Wu, Q.; Li, J.; Xiao, X.; Lott, A.; Lu, W.; Sheldon, B. W.; Wu, J., Silicon-Based Nanomaterials for Lithium-Ion Batteries: A Review. *Adv. Energy Mater.* **2014,** *4* (1), 1300882.
[12] Wu, F.; Maier, J.; Yu, Y., Guidelines and trends for next-generation rechargeable lithium and lithium-ion batteries. *Chem. Soc. Rev.* **2020,** *49* (5), 1569-1614.
[13] Nakajima, T.; Gupta, V.; Ohzawa, Y.; Koh, M.; Singh, R. N.; Tressaud, A.; Durand, E., Electrochemical behavior of plasma-fluorinated graphite for lithium ion batteries. *J. Power Sources* **2002,** *104* (1), 108-114.
[14] Aldon, L.; Kubiak, P.; Womes, M.; Jumas, J. C.; Olivier-Fourcade, J.; Tirado, J. L.; Corredor, J. I.; Pérez Vicente, C., Chemical and Electrochemical Li-Insertion into the $Li_4Ti_5O_{12}$ Spinel. *Chem. Mater.* **2004,** *16* (26), 5721-5725.
[15] Chaudhari, N. K.; Kim, M.-S.; Bae, T.-S.; Yu, J.-S., Hematite (α-Fe_2O_3) nanoparticles on vulcan carbon as an ultrahigh capacity anode material in lithium ion battery. *Electrochim. Acta* **2013,** *114*, 60-67.
[16] Wang, C. S.; Wu, G. T.; Zhang, X. B.; Qi, Z. F.; Li, W. Z., Lithium Insertion in Carbon-Silicon Composite Materials Produced by Mechanical Milling. *J. Electrochem. Soc.* **1998,** *145* (8), 2751-2758.

[17] Etxebarria, A.; Koch, S. L.; Bondarchuk, O.; Passerini, S.; Teobaldi, G.; Muñoz-Márquez, M. Á., Work Function Evolution in Li Anode Processing. *Adv. Energy Mater.* **2020,** *10* (24), 2000520.
[18] Obrovac, M. N.; Chevrier, V. L., Alloy negative electrodes for Li-ion batteries. *Chem. Rev.* **2014,** *114* (23), 11444-11502.
[19] Lyu, Y.; Wu, X.; Wang, K.; Feng, Z.; Cheng, T.; Liu, Y.; Wang, M.; Chen, R.; Xu, L.; Zhou, J.; Lu, Y.; Guo, B., An Overview on the Advances of $LiCoO_2$ Cathodes for Lithium-Ion Batteries. *Adv. Energy Mater.* **2020,** *11* (2), 2000982.
[20] Amatucci, G. G.; Tarascon, J. M.; Klein, C., CoO_2, The End Member of the Li_xCoO_2 Solid Solution. *J. Electrochem. Soc.* **1996,** *143* (3), 1114-1123.
[21] Reimers, J. N.; Dahn, J. R., Electrochemical and In Situ X-Ray Diffraction Studies of Lithium Intercalation in Li_xCoO_2. *J. Electrochem. Soc.* **1992,** *139* (8), 2091-2097.
[22] Chakraborty, A.; Kunnikuruvan, S.; Kumar, S.; Markovsky, B.; Aurbach, D.; Dixit, M.; Major, D. T., Layered Cathode Materials for Lithium-Ion Batteries: Review of Computational Studies on $LiNi_{1-x-y}Co_xMn_yO_2$ and $LiNi_{1-x-y}Co_xAl_yO_2$. *Chem. Mater.* **2020,** *32* (3), 915-952.
[23] Thackeray, M. M.; David, W. I. F.; Bruce, P. G.; Goodenough, J. B., Lithium insertion into manganese spinels. *Mater. Res. Bull.* **1983,** *18* (4), 461-472.
[24] Zhong, Q.; Bonakclarpour, A.; Zhang, M.; Gao, Y.; Dahn, J. R., Synthesis and Electrochemistry of $LiNi_xMn_{2-x}O_4$. *J. Electrochem. Soc.* **1997,** *144* (1), 205-213.
[25] Padhi, A. K.; Nanjundaswamy, K. S.; Goodenough, J. B., Phospho-olivines as Positive-Electrode Materials for Rechargeable Lithium Batteries. *J. Electrochem. Soc.* **1997,** *144* (4), 1188-1194.
[26] Manthiram, A., A reflection on lithium-ion battery cathode chemistry. *Nat. Commun.* **2020,** *11* (1), 1550.
[27] Li, B.; Xia, D., Anionic Redox in Rechargeable Lithium Batteries. *Adv. Mater.* **2017,** *29* (48), 1701054.
[28] Chen, J.; Deng, W.; Gao, X.; Yin, S.; Yang, L.; Liu, H.; Zou, G.; Hou, H.; Ji, X., Demystifying the Lattice Oxygen Redox in Layered Oxide Cathode Materials of Lithium-Ion Batteries. *ACS Nano* **2021,** *15* (4), 6061–6104.
[29] Kyerematen, N. A.; Hahn, R., Attainable Energy Density of Microbatteries. *ACS Energy Lett.* **2018,** *3* (5), 1172-1175.
[30] Cao, X.; Qiao, Y.; Jia, M.; He, P.; Zhou, H., Ion-Exchange: A Promising Strategy to Design Li-Rich and Li-Excess Layered Cathode Materials for Li-Ion Batteries. *Adv. Energy Mater.* **2021**, 2003972.
[31] Liu, J.; Wang, J.; Ni, Y.; Zhang, K.; Cheng, F.; Chen, J., Recent breakthroughs and perspectives of high-energy layered oxide cathode materials for lithium ion batteries. *Mater. Today* **2020,** *43*, 132-165.
[32] Qiu, B.; Zhang, M.; Xia, Y.; Liu, Z.; Meng, Y. S., Understanding and Controlling Anionic Electrochemical Activity in High-Capacity Oxides for Next Generation Li-Ion Batteries. *Chem. Mater.* **2017,** *29* (3), 908-915.

[33] Jarvis, K. A.; Deng, Z.; Allard, L. F.; Manthiram, A.; Ferreira, P. J., Atomic Structure of a Lithium-Rich Layered Oxide Material for Lithium-Ion Batteries: Evidence of a Solid Solution. *Chem. Mater.* **2011,** *23* (16), 3614-3621.
[34] Lee, S. H.; Moon, J.-S.; Lee, M.-S.; Yu, T.-H.; Kim, H.; Park, B. M., Enhancing phase stability and kinetics of lithium-rich layered oxide for an ultra-high performing cathode in Li-ion batteries. *J. Power Sources* **2015,** *281*, 77-84.
[35] Okubo, M.; Yamada, A., Molecular Orbital Principles of Oxygen-Redox Battery Electrodes. *ACS Appl. Energy Mater.* **2017,** *9* (42), 36463-36472.
[36] Ben Yahia, M.; Vergnet, J.; Saubanere, M.; Doublet, M. L., Unified picture of anionic redox in Li/Na-ion batteries. *Nat. Mater.* **2019,** *18* (5), 496-502.
[37] Boisse, B. M. d.; Nishimura, S. i.; Watanabe, E.; Lander, L.; Tsuchimoto, A.; Kikkawa, J.; Kobayashi, E.; Asakura, D.; Okubo, M.; Yamada, A., Highly Reversible Oxygen-Redox Chemistry at 4.1 V in $Na_{4/7-x}[\square_{1/7}Mn_{6/7}]O_2$ (□: Mn Vacancy). *Adv. Energy Mater.* **2018,** *8* (20), 1800409.
[38] Maitra, U.; House, R. A.; Somerville, J. W.; Tapia-Ruiz, N.; Lozano, J. G.; Guerrini, N.; Hao, R.; Luo, K.; Jin, L.; Pérez-Osorio, M. A.; Massel, F.; Pickup, D. M.; Ramos, S.; Lu, X.; McNally, D. E.; Chadwick, A. V.; Giustino, F.; Schmitt, T.; Duda, L. C.; Roberts, M. R.; Bruce, P. G., Oxygen redox chemistry without excess alkali-metal ions in $Na_{2/3}[Mg_{0.28}Mn_{0.72}]O_2$. *Nat. Chem.* **2018,** *10* (3), 288.
[39] Bai, X.; Sathiya, M.; Mendoza-Sánchez, B.; Iadecola, A.; Vergnet, J.; Dedryvère, R.; Saubanère, M.; Abakumov, A. M.; Rozier, P.; Tarascon, J.-M., Anionic Redox Activity in a Newly Zn-Doped Sodium Layered Oxide P2-$Na_{2/3}Mn_{1-y}Zn_yO_2$ ($0 < y < 0.23$). *Adv. Energy Mater.* **2018,** *8* (32), 1802379.
[40] Assat, G.; Tarascon, J.-M., Fundamental understanding and practical challenges of anionic redox activity in Li-ion batteries. *Nat. Energy* **2018,** *3* (5), 373–386.
[41] Chen, Q.; Pei, Y.; Chen, H.; Song, Y.; Zhen, L.; Xu, C. Y.; Xiao, P.; Henkelman, G., Highly reversible oxygen redox in layered compounds enabled by surface polyanions. *Nat. Commun.* **2020,** *11* (1), 3411.
[42] Chen, H.; Islam, M. S., Lithium extraction mechanism in Li-rich Li_2MnO_3 involving oxygen hole formation and dimerization. *Chem. Mater.* **2016,** *28* (18), 6656-6663.
[43] Rana, J.; Papp, J. K.; Lebens-Higgins, Z.; Zuba, M.; Kaufman, L. A.; Goel, A.; Schmuch, R.; Winter, M.; Whittingham, M. S.; Yang, W.; McCloskey, B. D.; Piper, L. F. J., Quantifying the Capacity Contributions during Activation of Li_2MnO_3. *ACS Energy Lett.* **2020,** *5* (2), 634-641.
[44] Francis Amalraj, S.; Markovsky, B.; Sharon, D.; Talianker, M.; Zinigrad, E.; Persky, R.; Haik, O.; Grinblat, J.; Lampert, J.; Schulz-Dobrick, M.; Garsuch, A.; Burlaka, L.; Aurbach, D., Study of the electrochemical behavior of the "inactive" Li_2MnO_3. *Electrochim. Acta* **2012,** *78*, 32-39.
[45] Kang, K.; Meng, Y. S.; Bre´ger, J.; Grey, C. P.; Ceder, G., Electrodes with High Power and High Capacity for Rechargeable Lithium Batteries. *Science* **2006,** *311* (5763), 977-980.
[46] Yan, P.; Nie, A.; Zheng, J.; Zhou, Y.; Lu, D.; Zhang, X.; Xu, R.; Belharouak, I.; Zu, X.; Xiao, J.; Amine, K.; Liu, J.; Gao, F.; Shahbazian-Yassar, R.; Zhang, J. G.; Wang,

C. M., Evolution of lattice structure and chemical composition of the surface reconstruction layer in $Li_{1.2}Ni_{0.2}Mn_{0.6}O_2$ cathode material for lithium ion batteries. *Nano Lett.* **2015,** *15* (1), 514-522.

[47] Vinckeviciute, J.; Kitchaev, D. A.; Van der Ven, A., A Two-Step Oxidation Mechanism Controlled by Mn Migration Explains the First-Cycle Activation Behavior of Li_2MnO_3-Based Li-Excess Materials. *Chem. Mater.* **2021,** *33* (5), 1625-1636.

[48] Eum, D.; Kim, B.; Kim, S. J.; Park, H.; Wu, J.; Cho, S. P.; Yoon, G.; Lee, M. H.; Jung, S. K.; Yang, W.; Seong, W. M.; Ku, K.; Tamwattana, O.; Park, S. K.; Hwang, I.; Kang, K., Voltage decay and redox asymmetry mitigation by reversible cation migration in lithium-rich layered oxide electrodes. *Nat. Mater.* **2020,** *19* (4), 419–427.

[49] Mohanty, D.; Mazumder, B.; Devaraj, A.; Sefat, A. S.; Huq, A.; David, L. A.; Payzant, E. A.; Li, J.; Wood, D. L.; Daniel, C., Resolving the degradation pathways in high-voltage oxides for high-energy-density lithium-ion batteries; Alternation in chemistry, composition and crystal structures. *Nano Energy* **2017,** *36*, 76-84.

[50] Bettge, M.; Li, Y.; Gallagher, K.; Zhu, Y.; Wu, Q.; Lu, W.; Bloom, I.; Abraham, D. P., Voltage Fade of Layered Oxides: Its Measurement and Impact on Energy Density. *J. Electrochem. Soc.* **2013,** *160* (11), A2046-A2055.

[51] Gent, W. E.; Lim, K.; Liang, Y.; Li, Q.; Barnes, T.; Ahn, S.-J.; Stone, K. H.; McIntire, M.; Hong, J.; Song, J. H.; Li, Y.; Mehta, A.; Ermon, S.; Tyliszczak, T.; Kilcoyne, D.; Vine, D.; Park, J.-H.; Doo, S.-K.; Toney, M. F.; Yang, W.; Prendergast, D.; Chueh, W. C., Coupling between oxygen redox and cation migration explains unusual electrochemistry in lithium-rich layered oxides. *Nat. Commun.* **2017,** *8* (1), 2091.

[52] Gu, M.; Belharouak, I.; Zheng, J.; Wu, H.; Xiao, J.; Genc, A.; Amine, K.; Thevuthasan, S.; Baer, D. R.; Zhang, J.-G.; Browning, N. D.; Liu, J.; Wang, C., Formation of the Spinel Phase in the Layered Composite Cathode Used in Li-Ion Batteries. *ACS Nano* **2013,** *7* (1), 760–767.

[53] Clearfield, A., Role of Ion Exchange in Solid-State Chemistry. *Chem. Rev.* **1988,** *88* (1), 125-148.

[54] Paulsen, J. M.; Thomas, C. L.; Dahn, J. R., O2 Structure $Li_{2/3}[Ni_{1/3}Mn_{2/3}]O_2$: A New Layered Cathode Material for Rechargeable Lithium Batteries I. Electrochemical Properties. *J. Electrochem. Soc.* **2000,** *147* (3), 861-868.

[55] Paulsen, J. M.; Dahn, J. R., O2-Type $Li_{2/3}[Ni_{1/3}Mn_{2/3}]O_2$: A New Layered Cathode Material for Rechargeable Lithium Batteries II. Structure, Composition, and Properties. *J. Electrochem. Soc.* **2000,** *147* (7), 2478-2485.

[56] Paulsen, J. M.; Larcher, D.; Dahn, J. R., O2 Structure $Li_{2/3}[Ni_{1/3}Mn_{2/3}]O_2$: A New Layered Cathode Material for Rechargeable Lithium Batteries III. Ion Exchange. *J. Electrochem. Soc.* **2000,** *147* (8), 2862-2867

[57] Jo, J. H.; Choi, J. U.; Park, Y. J.; Jung, Y. H.; Ahn, D.; Jeon, T. Y.; Kim, H.; Kim, J.; Myung, S. T., P2-$K_{0.75}[Ni_{1/3}Mn_{2/3}]O_2$ Cathode Material for High Power and Long Life Potassium-Ion Batteries. *Adv. Energy Mater.* **2020,** *10* (7), 1903605.

[58] Kim, H.; Kwon, D.-H.; Kim, J. C.; Ouyang, B.; Kim, H.; Yang, J.; Ceder, G., Na+ redistribution by electrochemical Na^+/K^+ exchange in layered $Na_xNi_2SbO_6$. *Chem. Mater.* **2020,** *32* (10), 4312–4323.

[59] Gwon, H.; Kim, S. W.; Park, Y. U.; Hong, J.; Ceder, G.; Jeon, S.; Kang, K., Ion-exchange mechanism of layered transition-metal oxides: case study of $LiNi_{0.5}Mn_{0.5}O_2$. *Inorg. Chem.* **2014,** *53* (15), 8083-8087.
[60] J. M. Paulsen, C. L. T., and J. R. Dahn, Layered Li-Mn-Oxide with the O2 Structure: A Cathode Material for Li-Ion Cells Which Does Not Convert to Spinel. *J. Electrochem. Soc.* **1999,** *146* (10), 3560-3565.
[61] Stoyanova, R.; Carlier, D.; Sendova-Vassileva, M.; Yoncheva, M.; Zhecheva, E.; Nihtianova, D.; Delmas, C., Stabilization of over-stoichiometric Mn^{4+} in layered $Na_{2/3}MnO_2$. *J. Solid State Chem.* **2010,** *183* (6), 1372-1379.
[62] Cao, X.; Li, H.; Qiao, Y.; Jia, M.; He, P.; Cabana, J.; Zhou, H., Achieving stable anionic redox chemistry in Li-excess O2-type layered oxide cathode via chemical ion-exchange strategy. *Energy Storage Mater.* **2021,** *38*, 1-8.
[63] Paulsen, J. M.; Mueller-Neuhaus, J. R.; Dahn, J. R., Layered $LiCoO_2$ with a Different Oxygen Stacking (O2 Structure) as a Cathode Material for Rechargeable Lithium Batteries. *J. Electrochem. Soc.* **2000,** *147* (2), 508-516
[64] Yabuuchi, N.; Hara, R.; Kajiyama, M.; Kubota, K.; Ishigaki, T.; Hoshikawa, A.; Komaba, S., New O2/P2-type Li-Excess Layered Manganese Oxides as Promising Multi-Functional Electrode Materials for Rechargeable Li/Na Batteries. *Adv. Energy Mater.* **2014,** *4* (13), 1301453.
[65] Tournadre, F.; Croguennec, L.; Saadoune, I.; Carlier, D.; Shao-Horn, Y.; Willmann, P.; Delmas, C., On the mechanism of the $P2–Na_{0.70}CoO_2 \rightarrow O2–LiCoO_2$ exchange reaction—Part I: proposition of a model to describe the P2–O2 transition. *J. Solid State Chem.* **2004,** *177* (8), 2790-2802.
[66] Tournadre, F.; Croguennec, L.; Willmann, P.; Delmas, C., On the mechanism of the $P2–Na_{0.70}CoO_2 \rightarrow O2–LiCoO_2$ exchange reaction—Part II: an in situ X-ray diffraction study. *J. Solid State Chem.* **2004,** *177* (8), 2803-2809.
[67] Paulsen J. M.; Dahn J. R., Studies of the layered manganese bronzes, $Na_{2/3}[Mn_{1-x}M_x]O_2$ with M=Co, Ni, Li, and $Li_{2/3}[Mn_{1-x}M_x]O_2$ prepared by ion-exchange. *Solid State Ion.* **1999,** *126* (1–2), 3-24.
[68] Shimoda, K.; Oishi, M.; Matsunaga, T.; Murakami, M.; Yamanaka, K.; Arai, H.; Ukyo, Y.; Uchimoto, Y.; Ohta, T.; Matsubara, E.; Ogumi, Z., Direct observation of layered-to-spinel phase transformation in Li_2MnO_3 and the spinel structure stabilised after the activation process. *J. Mater. Chem. A* **2017,** *5* (14), 6695-6707.
[69] Venkateswara Rao, C.; Soler, J.; Katiyar, R.; Shojan, J.; West, W. C.; Katiyar, R. S., Investigations on Electrochemical Behavior and Structural Stability of $Li_{1.2}Mn_{0.54}Ni_{0.13}Co_{0.13}O_2$ Lithium-Ion Cathodes via in-Situ and ex-Situ Raman Spectroscopy. *J. Phys. Chem. C* **2014,** *118* (26), 14133-14141.
[70] Amalraj, S. F.; Sharon, D.; Talianker, M.; Julien, C. M.; Burlaka, L.; Lavi, R.; Zhecheva, E.; Markovsky, B.; Zinigrad, E.; Kovacheva, D.; Stoyanova, R.; Aurbach, D., Study of the nanosized Li_2MnO_3: Electrochemical behavior, structure, magnetic properties, and vibrational modes. *Electrochim. Acta* **2013,** *97*, 259-270.
[71] Amalraj, S. F.; Burlaka, L.; Julien, C. M.; Mauger, A.; Kovacheva, D.; Talianker, M.; Markovsky, B.; Aurbach, D., Phase Transitions in Li_2MnO_3 Electrodes at Various States-of-Charge. *Electrochim. Acta* **2014,** *123*, 395-404.

[72] Qiao, Y.; Guo, S.; Zhu, K.; Liu, P.; Li, X.; Jiang, K.; Sun, C.-J.; Chen, M.; Zhou, H., Reversible anionic redox activity in Na_3RuO_4 cathodes: a prototype Na-rich layered oxide. *Energy Environ. Sci.* **2018,** *11* (2), 299-305.
[73] Li, X.; Qiao, Y.; Guo, S.; Xu, Z.; Zhu, H.; Zhang, X.; Yuan, Y.; He, P.; Ishida, M.; Zhou, H., Direct Visualization of the Reversible O^{2-}/O^{-} Redox Process in Li-Rich Cathode Materials. *Adv. Mater.* **2018,** *30* (14), 1705197.
[74] Cao, X.; Li, X.; Qiao, Y.; Jia, M.; Qiu, F.; He, Y.; He, P.; Zhou, H., Restraining Oxygen Loss and Suppressing Structural Distortion in a Newly Ti-Substituted Layered Oxide P2-$Na_{0.66}Li_{0.22}Ti_{0.15}Mn_{0.63}O_2$. *ACS Energy Lett.* **2019,** *4* (10), 2409-2417.
[75] Cao, X.; Li, H.; Qiao, Y.; Li, X.; Jia, M.; Cabana, J.; Zhou, H., Stabilizing Reversible Oxygen Redox Chemistry in Layered Oxides for Sodium-Ion Batteries. *Adv. Energy Mater.* **2020,** *10* (15), 1903785.
[76] Li, N.; Hwang, S.; Sun, M.; Fu, Y.; Battaglia, V. S.; Su, D.; Tong, W., Unraveling the Voltage Decay Phenomenon in Li-Rich Layered Oxide Cathode of No Oxygen Activity. *Adv. Energy Mater.* **2019,** *9* (47), 1902258.
[77] Dau, H.; Liebisch, P.; Haumann, M., X-ray absorption spectroscopy to analyze nuclear geometry and electronic structure of biological metal centers--potential and questions examined with special focus on the tetra-nuclear manganese complex of oxygenic photosynthesis. *Anal. Bioanal. Chem.* **2003,** *376* (5), 562-83.
[78] Wang, Q.; Mariyappan, S.; Rousse, G.; Morozov, A. V.; Porcheron, B.; Dedryvère, R.; Wu, J.; Yang, W.; Zhang, L.; Chakir, M.; Avdeev, M.; Deschamps, M.; Yu, Y.-S.; Cabana, J.; Doublet, M.-L.; Abakumov, A. M.; Tarascon, J.-M., Unlocking anionic redox activity in O3-type sodium 3d layered oxides via Li substitution. *Nat. Mater.* **2021,** *20* (3), 353-361.
[79] Grimaud, A.; Hong, W. T.; Shao-Horn, Y.; Tarascon, J. M., Anionic redox processes for electrochemical devices. *Nat. Mater.* **2016,** *15* (2), 121-126.
[80] Luo, K.; Roberts, M. R.; Guerrini, N.; Tapia-Ruiz, N.; Hao, R.; Massel, F.; Pickup, D. M.; Ramos, S.; Liu, Y. S.; Guo, J.; Chadwick, A. V.; Duda, L. C.; Bruce, P. G., Anion Redox Chemistry in the Cobalt Free 3d Transition Metal Oxide Intercalation Electrode $Li[Li_{0.2}Ni_{0.2}Mn_{0.6}]O_2$. *J. Am. Chem. Soc.* **2016,** *138* (35), 11211-11218.
[81] Robertson, A. D.; Bruce, P. G., Mechanism of electrochemical activity in Li2MnO3. *Chem. Mater.* **2003,** *15* (10), 1984-1992.
[82] Song, J.; Li, B.; Chen, Y.; Zuo, Y.; Ning, F.; Shang, H.; Feng, G.; Liu, N.; Shen, C.; Ai, X.; Xia, D., A High-Performance Li-Mn-O Li-rich Cathode Material with Rhombohedral Symmetry via Intralayer Li/Mn Disordering. *Adv. Mater.* **2020,** *32* (16), 2000190.
[83] Heubner, C.; Lein, T.; Schneide, M.; Michaelis, A., Intercalation Materials for Secondary Batteries Based on Alkali Metal Exchange: Developments and Perspectives. *J. Mater. Chem. A* **2020,** *8* (33), 16854-16883.
[84] Li, X.; Qiao, Y.; Guo, S.; Jiang, K.; Ishida, M.; Zhou, H., A New Type of Li-Rich Rock-Salt Oxide $Li_2Ni_{1/3}Ru_{2/3}O_3$ with Reversible Anionic Redox Chemistry. *Adv. Mater.* **2019,** *31* (11), 1807825.
[85] Ning, F.; Li, B.; Song, J.; Zuo, Y.; Shang, H.; Zhao, Z.; Yu, Z.; Chu, W.; Zhang, K.; Feng, G.; Wang, X.; Xia, D., Inhibition of oxygen dimerization by local symmetry

tuning in Li-rich layered oxides for improved stability. *Nat. Commun.* **2020,** *11* (1), 4973.

[86] Taylor, Z. N.; Perez, A. J.; Coca-Clemente, J. A.; Braga, F.; Drewett, N. E.; Pitcher, M. J.; Thomas, W. J.; Dyer, M. S.; Collins, C.; Zanella, M.; Johnson, T.; Day, S.; Tang, C.; Dhanak, V. R.; Claridge, J. B.; Hardwick, L. J.; Rosseinsky, M. J., Stabilization of O-O Bonds by d^0 Cations in $Li_{4+x}Ni_{1-x}WO_6$ ($0 \leq x \leq 0.25$) Rock Salt Oxides as the Origin of Large Voltage Hysteresis. *J. Am. Chem. Soc.* **2019,** *141* (18), 7333-7346.

[87] Cao, X.; Li, H.; Qiao, Y.; Jia, M.; Li, X.; Cabana, J.; Zhou, H., Stabilizing Anionic Redox Chemistry in a Mn-Based Layered Oxide Cathode Constructed by Li-Deficient Pristine State. *Adv. Mater.* **2020**, 2004280.

[88] Teufl, T.; Strehle, B.; Müller, P.; Gasteiger, H. A.; Mendez, M. A., Oxygen Release and Surface Degradation of Li- and Mn-Rich Layered Oxides in Variation of the Li_2MnO_3 Content. *J. Electrochem. Soc.* **2018,** *165* (11), A2718-A2731.

[89] Guerrini, N.; Jin, L.; Lozano, J. G.; Luo, K.; Sobkowiak, A.; Tsuruta, K.; Massel, F.; Duda, L.-C.; Roberts, M. R.; Bruce, P. G., Charging Mechanism of Li_2MnO_3. *Chem. Mater.* **2020,** *32* (9), 3733-3740.

[90] Saubanere, M.; McCalla, E.; Tarascon, J. M.; Doublet, M. L., The intriguing question of anionic redox in high-energy density cathodes for Li-ion batteries. *Energy Environ. Sci.* **2016,** *9* (3), 984-991.

[91] House, R. A.; Maitra, U.; Pérez-Osorio, M. A.; Lozano, J. G.; Jin, L.; Somerville, J. W.; Duda, L. C.; Nag, A.; Walters, A.; Zhou, K.; Roberts, M. R.; Bruce, P. G., Superstructure control of first-cycle voltage hysteresis in O-redox cathodes. *Nature* **2019,** *577* (7791), 502–508.

[92] Carlier, D.; Ménétrier, M.; Grey, C. P.; Delmas, C.; Ceder, G., Understanding the NMR shifts in paramagnetic transition metal oxides using density functional theory calculations. *Phys. Rev. B* **2003,** *67* (17), 174103.

[93] Hung, I.; Zhou, L.; Pourpoint, F.; Grey, C. P.; Gan, Z., Isotropic high field NMR spectra of Li-ion battery materials with anisotropy >1 MHz. *J. Am. Chem. Soc.* **2012,** *134* (4), 1898-1901.

[94] Cabana, J.; Casas-Cabanas, M.; Omenya, F. O.; Chernova, N. A.; Zeng, D.; Whittingham, M. S.; Grey, C. P., Composition-structure relationships in the Li-ion battery electrode material $LiNi_{0.5}Mn_{1.5}O_4$. *Chem. Mater.* **2012,** *24* (15), 2952-2964.

[95] Oishi, M.; Yamanaka, K.; Watanabe, I.; Shimoda, K.; Matsunaga, T.; Arai, H.; Ukyo, Y.; Uchimoto, Y.; Ogumi, Z.; Ohta, T., Direct observation of reversible oxygen anion redox reaction in Li-rich manganese oxide, Li_2MnO_3, studied by soft X-ray absorption spectroscopy. *J. Mater. Chem. A* **2016,** *4* (23), 9293-9302.

[96] Jia, M.; Li, H.; Qiao, Y.; Wang, L.; Cao, X.; Cabana, J.; Zhou, H., Elucidating Anionic Redox Chemistry in P3 Layered Cathode for Na-Ion Batteries. *ACS Appl. Mater. & Interfaces* **2020,** *12* (34), 38249-38255.

[97] Sudayama, T.; Uehara, K.; Mukai, T.; Asakura, D.; Shi, X.-M.; Tsuchimoto, A.; Mortemard de Boisse, B.; Shimada, T.; Watanabe, E.; Harada, Y.; Nakayama, M.; Okubo, M.; Yamada, A., Multiorbital bond formation for stable oxygen-redox reaction in battery electrodes. *Energy Environ. Sci.* **2020,** *13* (5), 1492-1500.

[98] Naylor, A. J.; Makkos, E.; Maibach, J.; Guerrini, N.; Sobkowiak, A.; Björklund, E.; Lozano, J. G.; Menon, A. S.; Younesi, R.; Roberts, M. R.; Edström, K.; Islam, M. S.; Bruce, P. G., Depth-dependent oxygen redox activity in lithium-rich layered oxide cathodes. *J. Mater. Chem. A* **2019,** *7* (44), 25355-25368.
[99] Hy, S.; Su, W.-N.; Chen, J.-M.; Hwang, B.-J., Soft X-ray Absorption Spectroscopic and Raman Studies on $Li_{1.2}Ni_{0.2}Mn_{0.6}O_2$ for Lithium-Ion Batteries. *J. Phys. Chem. C* **2012,** *116* (48), 25242-25247.
[100] Thackeray, M. M.; Kang, S.-H.; Johnson, C. S.; Vaughey, J. T.; Benedek, R.; Hackney, S. A., Li_2MnO_3-stabilized $LiMO_2$ (M = Mn, Ni, Co) electrodes for lithium-ion batteries. *J. Mater. Chem.* **2007,** *17* (30), 3112-3125.
[101] Yabuuchi, N.; Yoshii, K.; Myung, S.-T.; Nakai, I.; Komaba, S., Detailed studies of a high-capacity electrode material for rechargeable batteries, Li_2MnO_3–$LiCo_{1/3}Ni_{1/3}Mn_{1/3}O2$. *J. Am. Chem. Soc.* **2011,** *133* (12), 4404-4419.